

Università degli studi di Padova
Dipartimento di Fisica e Astronomia

Tesi di Dottorato

Search for heavy resonances decaying into a Z boson and a vector boson in the $\nu\bar{\nu} q\bar{q}$ final state at CMS

Supervisor: Prof. Franco Simonetto
Candidate: Lisa Benato

Scuola di Dottorato di Ricerca, XXX ciclo

"I have no special talent. I am only passionately curious."
(A. Einstein)

Contents

1	Introduction	1
2	Theoretical motivation	3
2.1	Beyond Standard Model theories	3
2.2	Heavy Vector Triplet	5
2.2.1	Simplified Lagrangian	5
2.2.2	Mass eigenstates, mixing parameters and decay widths	6
2.2.3	HVT production	9
2.2.4	Benchmark model A: weak coupling scenario	11
2.2.5	Benchmark model B: strong coupling scenario	12
2.2.6	Search for HVT resonances at LHC	12
2.3	Warped extra dimension	16
2.3.1	Randall-Sundrum original model (RS1)	16
2.3.2	Bulk extension of RS1: graviton production and decays	19
2.3.3	Search for KK bulk gravitons at LHC	22
3	The Large Hadron Collider and the CMS experiment	25
3.1	The Large Hadron Collider	25
3.1.1	Proton-proton interactions	28
3.2	CMS detector	29
3.2.1	The coordinate system	29
3.2.2	The magnet	30
3.2.3	The tracking system	31
3.2.4	The electromagnetic calorimeter	34
3.2.5	The hadronic calorimeter	34
3.2.6	The muon system	35
3.2.7	The trigger system and data acquisition	37
3.2.8	Particle Flow event reconstruction	38
3.2.9	Physics objects	38
3.3	ATLAS, ALICE, LHCb detectors	46
3.3.1	ATLAS	46
3.3.2	ALICE	47
3.3.3	LHCb	47

4	Search for diboson resonances in the $ZV \rightarrow \nu\bar{\nu}q\bar{q}$ final state	49
4.1	Data and Monte Carlo samples	50
4.2	Event selection	51
4.2.1	Vertex and Pile-up	51
4.2.2	Electrons	51
4.2.3	Muons	52
4.2.4	Taus	53
4.2.5	Photons	54
4.2.6	Jets	55
4.2.7	Jet mass	57
4.2.8	Jet substructure	58
4.2.9	b-tagging	58
4.2.10	Missing Energy	59
4.3	Diboson candidate reconstruction	61
4.4	Background estimation	62
4.5	Systematic uncertainties	63
4.6	Results	64
5	Combination of diboson searches in semileptonic final states	65
6	Conclusions	67

1

Abstract

2

3

CONTENTS

Introduction

7 This analysis searches for signal of heavy resonances decaying into a pair of heavy vector bosons.
8 One Z boson is identified through its invisible decay ($\nu\nu$), while the other is required to decay hadron-
9 ically into a pair of quarks. The final states probed by this analysis therefore consists in two quarks
10 and two neutrinos, reconstructed as missing transverse energy (met). The hadronically decaying
11 boson (Z, W) is reconstructed as a fat jet, whose mass is used to define the signal region. Two purity
12 categories are exploited, based on the n-subjettiness of the fat jet.

13 The search is performed by examining the distribution of the diboson reconstructed transverse
14 mass of the resonance VZ (mtVZ) for a localized excess. The shape and normalization of the main
15 background of the analysis (V+jets) are estimated with an hybrid approach using the distribution
16 of data in the sidebands, corrected for a function accounting for potential differences between the
17 signal region and the sidebands, while the minor background sources are taken from simulations.

Theoretical motivation

21 The standard model (SM) of particles represents, so far, the best available description of the parti-
 22 cles and their interactions. It is the summation of two gauge theories: the electroweak interaction,
 23 that portrays the weak and electromagnetic interactions together, and the strong interaction, or
 24 Quantum Chromodynamics (QCD). Particles, namely quarks and leptons, are described as spin 1/2
 25 fermions, whilst interactions are represented by spin 1 bosons. The symmetry group of the standard
 26 model is:

$$SU_C(3) \times SU_L(2) \times U_Y(1), \quad (2.1)$$

27 where the first factor is related to strong interactions, whose mediators are eight gluons, while
 28 $SU_L(2) \times U_Y(1)$ is the electroweak symmetry group, whose mediators are photons and Z - W^\pm bosons.
 29 In renormalizable theories, with no anomalies, all gauge bosons are expected to be massless, in con-
 30 trast with our experimental knowledge. This inconsistency is solved by introducing a new scalar
 31 particle, the Higgs boson, that can give mass to weak bosons and fermions via the spontaneous
 32 symmetry breaking mechanism.

33
 34 In the last decades, Standard Model has been accurately probed by many experimental facilities
 35 (LEP, Tevatron, LHC), and the results lead to an impressive agreement between theoretical pre-
 36 dictions and experiments. The discovery of the Higgs boson at the CERN Large Hadron Collider,
 37 measured by both CMS and ATLAS collaborations [1–7], represents not only an extraordinary con-
 38 firmation of the model, but also the latest biggest achievement in particle physics as a whole.

39 2.1 Beyond Standard Model theories

- 40 Even though the Standard Model is the most complete picture of the universe of the particles, many
 41 questions are still left open. From a phenomenological point of view, some experimental observa-
 42 tions are not included in the theory:
- 43 • in SM, neutrinos are massless (whilst experimentally their masses are confirmed to be non-
 44 zero, i.e. by the neutrino oscillations);
 - 45 • no candidates for dark matter are predicted;
 - 46 • no one of the fields included in the SM can explain the cosmological inflation;

- 47 • SM can not justify the matter-antimatter asymmetry.
- 48 From a purely theoretical perspective, some issues are still relevant in the formulation of the model:
- 49 • *Flavour problem.*
- 50 The Standard Model has 18 free parameters: 9 fermionic masses; 3 angular parameters in
51 Cabibbo-Kobayashi-Maskawa matrix, plus 1 phase parameter; electromagnetic coupling α ;
52 strong coupling α_{strong} ; weak coupling α_{weak} ; Z mass; the mass of the Higgs boson. Such a
53 huge number of degrees of freedom marks the SM as weakly predictive in the flavour sector.
- 54 • *Unification.*
- 55 There is not a “complete” unification of strong, weak and electromagnetic interactions, since
56 each one has its own coupling constant, behaving differently at different energy scales; not to
57 mention the fact that gravitational interaction is completely excluded from the SM.
- 58 • *Hierarchy problem.*
- 59 From Quantum Field Theory, it is known that perturbative corrections to the mass of the scalar
60 bosons included in the theory tend to make it increase towards the energy scale at which the
61 considered theory still holds [8]. If the Standard Model is seen as a low-mass approximation of
62 a more general theory valid up to the Planck mass scale (*i.e.*, $\sim 1.2 \times 10^{19}$ GeV), a fine-tuning
63 cancellation of the order of 1 over 10^{34} is needed in order to protect the Higgs mass at the
64 electroweak scale (~ 100 GeV). Such an astonishing correction is perceived as very unnatural.
- 65 Numerous Beyond Standard Model theories (BSM) have been proposed in order to overcome
66 the limits of the Standard Model.
- 67 Grand Unified Theories (GUT) aim at extending the symmetry group of the SM (eq. 2) into largest
68 candidates, such as $SO(10)$, $SU(5)$ and $E(6)$. At GUT scale, approximately at 10^{16} GeV, non-gravitational
69 interactions are expected to be ruled by only one coupling constant, α_{GUT} .
- 70 Super Symmetry (SUSY) models state that every fermion (boson) of the Standard Model has a
71 bosonic (fermionic) superpartner, with exactly the same quantum numbers, except the spin. If
72 SUSY is not broken, each couple of partners and superpartners should have the same masses, hy-
73 pothesis excluded by the non-observation of the s-electron. Super Symmetry represents a very ele-
74 gant solution of the hierarchy problem of the Higgs boson mass, since the perturbative corrections
75 brought by new SUSY particles exactly cancel out the divergences caused by SM particles correc-
76 tions. A particular sub-class of SUSY models, Minimal Super Symmetric Standard Models, is char-
77 acterized by the introduction of a new symmetry, the R-parity, that guarantees the proton stability
78 and also the stability of the lightest SUSY particle, a possible good candidate for dark matter.
- 79
- 80 Two other possible theoretical pictures are extensively described in sec. 2.2-2.3.

2.2 Heavy Vector Triplet

81 2.2 Heavy Vector Triplet

82 The heavy vector triplet model [9] provides a general framework aimed at studying new physics be-
83 yond the standard model, that can manifest into the appearance of new resonances.
84 The adopted approach is that of the simplified model, in which an effective Lagrangian is intro-
85 duced, in order to describe the properties and interactions of new particles (in this case, a triplet of
86 spin-1 bosons) by using a limited set of parameters, that can be easily linked to the physical observ-
87 ables at the LHC experiments. These parameters can describe many physical motivated theories
88 (such as sequential extensions of the SM [10, 11] or Composite Higgs [12, 13]).
89 Since a simplified model is not a complete theory, its validity is restricted to the on-shell quanti-
90 ties related to the production and decay mechanisms of the new resonances, that is how most of
91 the LHC BSM searches are performed. Given these conditions, experimental results in the resonant
92 region are sensitive to a limited number of the phenomenological Lagrangian parameters (or to a
93 combination of those), whilst the remaining parameters tend to influence the tail of the distribu-
94 tions.
95 Limits on production cross-section times branching ratio ($\sigma \mathcal{B}$), as a function of the invariant mass
96 spectrum of the probed resonance, can be extracted from experimental data. Given that $\sigma \mathcal{B}$ are
97 functions of the simplified model parameters and of the parton luminosities, it is then possible to
98 interpret the observed limits in the parameter space.

99 2.2.1 Simplified Lagrangian

100 The heavy vector triplet framework assumes the existence of an additional vector triplet, V_μ^a , $a =$
101 1, 2, 3, in which two spin-1 particles are charged and one is neutral:

$$V_\mu^\pm = \frac{V_\mu^1 \mp i V_\mu^2}{\sqrt{2}}; \quad (2.2)$$
$$V_\mu^0 = V_\mu^3.$$

102
103 The triplet interactions are described by a simplified Lagrangian, that is invariant under SM gauge
104 and CP symmetry, and accidentally invariant under the custodial symmetry $SU(2)_L \times SU(2)_R$:

$$\begin{aligned} \mathcal{L}_V = & -\frac{1}{4} (D_\mu V_\nu^a - D_\nu V_\mu^a) (D^\mu V^\nu{}^a - D^\nu V^\mu{}^a) + \frac{m_V^2}{2} V_\mu^a V^\mu{}^a \\ & + i g_V c_H V_\mu^a (H^\dagger \tau^a D^\mu H - D^\mu H^\dagger \tau^a H) + \frac{g^2}{g_V} c_F V_\mu^a \sum_f \bar{f}_L \gamma^\mu \tau^a f_L \\ & + \frac{g_V}{2} c_{VVV} \epsilon_{abc} V_\mu^a V_\nu^b (D^\mu V^\nu{}^c - D^\nu V^\mu{}^c) + g_V^2 c_{VHH} V_\mu^a V^\mu{}^a H^\dagger H - \frac{g}{2} c_{VWW} \epsilon_{abc} W^{\mu\nu}{}^a V_\mu^b V_\nu^c. \end{aligned} \quad (2.3)$$

105
106 In the first line of the formula 2.3, V mass and kinematic terms are included, described with the co-
107 variant derivative $D_\mu V_\nu^a = \partial_\mu V_\nu^a + g \epsilon^{abc} W_\mu^b V_\nu^c$, where W_μ^a are the fields of the weak interaction and
108 g is the weak gauge coupling. V_μ^a are not mass eigenstates, since they mix with the electroweak fields
109 after the spontaneous symmetry breaking, therefore m_V isn't the physical mass of the V bosons.
110 The second line describes the interaction of the triplet with the Higgs field and the SM left-handed
111 fermions; c_H describes the vertices with the physical Higgs and the three unphysical Goldstone
112 bosons that, for the Goldstone equivalence theorem, are equivalent to the longitudinal polarization
113 of W and Z bosons at high-energy; hence, c_H is related to the bosonic decays of the resonances. c_F

114 is the analogous parameter describing the V interaction with fermions, that can be generalized as a
 115 flavour dependent coefficient, once defined $J_F^{\mu a} = \sum_f \bar{f}_L \gamma^\mu \tau^a f_L$: $c_F V_\mu^a J_F^{\mu a} = c_\ell V_\mu^a J_\ell^{\mu a} + c_q V_\mu^a J_q^{\mu a} +$
 116 $c_3 V_\mu^a J_3^{\mu a}$.

117 The last part of the equation includes terms that are relevant only in strongly coupled scenarios (see
 118 sec. 2.2.2.2) through the V - W mixing, but it does not include vertices of V with light SM fields, hence
 119 it can be neglected while describing the majority of the LHC phenomenology, under the assump-
 120 tions previously stated. Additional dimension four quadrilinear V interactions are non relevant for
 121 the processes discussed, otherwise their effects would be appreciated in electroweak precision tests
 122 and precise Higgs coupling measurements [14].

123
 124 The parameters in the Lagrangian can be interpreted as follows: g_V describes the strength of
 125 the interaction, that is weighted by c parameters. g_V ranges from $g_V \sim 1$ when the coupling is
 126 weak (sec. 2.2.4), to $g_V \sim 4\pi$ when the coupling is strong (sec. 2.2.5). c parameters are expected
 127 to be $c \sim 1$, except to c_H , that can be smaller for weak couplings. The combinations describing the
 128 vertices, $g_V c_H$ and $g^2/g_V c_F$, can be considered as the fundamental parameters, used to interpret
 129 the experimental results.

130 2.2.2 Mass eigenstates, mixing parameters and decay widths

131 The newly introduced $SU(2)_L$ triplet is expected to mix with the weak SM fields. The $U(1)_{em}$ sym-
 132 metry is left unbroken by the new interaction, hence the massless combination of the electroweak
 133 fields, namely the photon, is the same as the SM:

$$A_\mu = B_\mu \cos \theta_W + W_\mu^3 \sin \theta_W, \quad (2.4)$$

134 with the usual definitions of the electroweak parameters:

$$\begin{aligned} \tan \theta_W &= \frac{g'}{g} \\ e &= \frac{gg'}{\sqrt{g^2 + g'^2}} \\ g &= e / \sin \theta_w \\ g' &= e / \cos \theta_w. \end{aligned} \quad (2.5)$$

135 The Z boson, on the other hand, mixes with the neutral component of the triplet, V^0 , with a
 136 rotation parametrized with the angle θ_N :

$$\begin{pmatrix} \cos \theta_N & \sin \theta_N \\ -\sin \theta_N & \cos \theta_N d \end{pmatrix} \begin{pmatrix} Z \\ V^0 \end{pmatrix}. \quad (2.6)$$

137 The mass matrix of the rotated system is given by:

$$\mathbb{M}_N^2 = \begin{pmatrix} \hat{m}_Z^2 & c_H \zeta \hat{m}_Z \hat{m}_V \\ c_H \zeta \hat{m}_Z \hat{m}_V & \hat{m}_V^2 \end{pmatrix}, \quad (2.7)$$

138 where the parameters are defined as:

$$\left\{ \begin{array}{l} \hat{m}_Z = \frac{e}{2 \sin \theta_W \cos \theta_W} \hat{v} \\ \hat{m}_V^2 = m_V^2 + g_V^2 c_{VVHH} \hat{v}^2 \\ \zeta = \frac{g_V \hat{v}}{2 \hat{m}_V} \\ \frac{\hat{v}^2}{2} = \langle H^\dagger H \rangle \end{array} \right., \quad (2.8)$$

2.2 Heavy Vector Triplet

- ¹³⁹ and \hat{v} , the vacuum expectation value of the Higgs field, can be different from the SM $v = 246$ GeV.
¹⁴⁰ The physical masses of Z and V^0 , m_Z and M_0 , and θ_N come from the matrix relations:

$$\begin{aligned}\text{Tr}(\mathbb{M}_N^2) &= \hat{m}_Z^2 + \hat{m}_V^2 = m_Z^2 + M_0^2 \\ \|\mathbb{M}_N^2\| &= \hat{m}_Z^2 + \hat{m}_V^2 (1 - c_H^2 \zeta^2) = m_Z^2 M_0^2 \\ \tan 2\theta_N &= \frac{2c_H \zeta \hat{m}_Z \hat{m}_V}{\hat{m}_V^2 - \hat{m}_Z^2}.\end{aligned}\tag{2.9}$$

- ¹⁴¹ The W^\pm bosons mix with the charged components of the triplet, V^\pm , leading to a mass matrix
¹⁴² analogous to eq. 2.10:

$$\mathbb{M}_C^2 = \begin{pmatrix} \hat{m}_W^2 & c_H \zeta \hat{m}_W \hat{m}_V \\ c_H \zeta \hat{m}_W \hat{m}_V & \hat{m}_V^2 \end{pmatrix},\tag{2.10}$$

- ¹⁴³ where \hat{m}_W is defined as:

$$\left\{ \begin{array}{l} \hat{m}_W = \frac{e}{2 \sin \theta_W} \hat{v} = \hat{m}_Z \cos \theta_W \\ \end{array} \right.;\tag{2.11}$$

- ¹⁴⁴ the physical masses of W and V^\pm , m_W and M_\pm , and the angle θ_C parametrizing the rotation of the
¹⁴⁵ charged sector are described by:

$$\begin{aligned}\text{Tr}(\mathbb{M}_C^2) &= \hat{m}_W^2 + \hat{m}_V^2 = m_W^2 + M_\pm^2 \\ \|\mathbb{M}_C^2\| &= \hat{m}_W^2 + \hat{m}_V^2 (1 - c_H^2 \zeta^2) = m_W^2 M_\pm^2 \\ \tan 2\theta_C &= \frac{2c_H \zeta \hat{m}_W \hat{m}_V}{\hat{m}_V^2 - \hat{m}_W^2}.\end{aligned}\tag{2.12}$$

- ¹⁴⁶ The custodial symmetry of eq. 2.3 guarantees that:

$$\mathbb{M}_C^2 = \begin{pmatrix} \cos \theta_W & 0 \\ 0 & 1 \end{pmatrix} \mathbb{M}_N^2 \begin{pmatrix} \cos \theta_W & 0 \\ 0 & 1 \end{pmatrix}.\tag{2.13}$$

- ¹⁴⁷
- ¹⁴⁸ By taking the determinant of these matrices, a custodial relation among the masses can be extracted:
¹⁴⁹

$$m_W^2 M_\pm^2 = \cos \theta_W m_Z^2 M_0^2,\tag{2.14}$$

- ¹⁵⁰ that has some very important consequences.
¹⁵¹ Given that this model aims at searching new particles in the TeV scale and that the scale of the elec-
¹⁵² troweak interactions must lay at ~ 100 GeV, a hierarchy of the physical masses seems very natural:

$$\frac{\hat{m}_{(W,Z)}}{\hat{m}_V} \sim \frac{m_{(W,Z)}}{M_{(\pm,0)}} \ll 1;\tag{2.15}$$

- ¹⁵⁴ ζ parameter can be $\zeta \ll 1$ (weakly coupled scenario) or $\zeta \sim 1$ (strongly coupled scenario). When
¹⁵⁵ eq. 2.15 applies, the second lines in eq. 2.9 and eq. 2.12 can be approximated as follows:

$$\begin{aligned}m_Z^2 &= \hat{m}_Z^2 (1 - c_H^2 \zeta^2) (1 + \mathcal{O}(\hat{m}_Z^2 / \hat{m}_V^2)) \\ m_W^2 &= \hat{m}_W^2 (1 - c_H^2 \zeta^2) (1 + \mathcal{O}(\hat{m}_W^2 / \hat{m}_V^2)).\end{aligned}\tag{2.16}$$

- ¹⁵⁶
- ¹⁵⁷ From eq. 2.11, the ratio of the physical masses of the charged and neutral electroweak bosons can
¹⁵⁸ be approximated as:

$$\frac{m_W^2}{m_Z^2} \approx \cos \theta_W^2,\tag{2.17}$$

159 that satisfies the SM tree-level relation $\rho = 1$ if $\cos \theta_W^2 \approx 1. - 0.23$. Adding this approximation into
160 eq. 2.14, the V bosons are expected to have the same masses, hence the same production rates:

$$M_{\pm}^2 = M_0^2 (1 + \mathcal{O}(\%)). \quad (2.18)$$

161 The degenerate mass of the triplet will be called $M_V \approx M_{\pm} \approx M_0$; given 2.15, $M_V = \hat{m}_V$.
162 Another consequence of the mass hierarchy (2.15) is that the mixing angles $\theta_{(N,C)}$ between the elec-
163 troweak fields and the triplet are small:

$$\theta_{(N,C)} \approx c_H \zeta \frac{\hat{m}_{(W,Z)}}{\hat{m}_V} \ll 1, \quad (2.19)$$

164 hence the couplings among SM particles are very close to the couplings predicted by the SM.

165 2.2.2.1 Decay widths into fermions

166 The couplings among the triplet and SM fermions are expressed as a function of the rotation angles
167 $\theta_{(C,N)}$ and SM couplings (omitting the CKM matrix elements for quarks):

$$\begin{cases} g_L^N = \frac{g^2}{g_V} \frac{c_F}{2} \cos \theta_N + (g_L^Z)_{SM} \sin \theta_N \approx \frac{g^2}{g_V} \frac{c_F}{2}, \\ g_R^N = (g_R^Z)_{SM} \sin \theta_N \approx 0 \end{cases},$$

$$\begin{cases} g_L^C = \frac{g^2}{g_V} \frac{c_F}{2} \cos \theta_C + (g_L^W)_{SM} \sin \theta_N \approx \frac{g^2}{g_V} \frac{c_F}{2}, \\ g_R^C = 0 \end{cases}, \quad (2.20)$$

168 where $g_L^W = g/\sqrt{2}$; $g_{L,R}^{W,Z}$ are those predicted by the standard model. The V bosons interact with SM
169 left fermions, and the strength of the couplings with fermions is determined by $g^2/g_V c_F$, as stated
170 in sec. 2.2.1. The decay width into fermions is then given by:

$$\Gamma_{V^{\pm} \rightarrow f \bar{f}} \approx 2\Gamma_{V^0 \rightarrow f \bar{f}} \approx N_c \left(\frac{g^2 c_F}{g_V} \right)^2 \frac{M_V}{48\pi}, \quad (2.21)$$

171 where N_c is the number of colours (3 for quarks, 1 for leptons).

172 2.2.2.2 Decay widths into bosons

173 As a starting point, a proper choice of the gauge makes the derivation of the approximate decay
174 widths easier. While the unitary gauge is very convenient in discussing the electroweak symmetry
175 breaking mechanism, since it provides a basis in which the Goldstone components of the scalar
176 fields of the theory are set to zero, it does not properly describe the longitudinally polarized bosons
177 in high-energy regimes, since it introduces a dependence of the type E/m in the longitudinal po-
178 larization vector, not corresponding to the experimental results. This pathological behaviour can
179 be overcome profiting of the equivalence theorem: while calculating the scattering amplitude of
180 an high-energy process, the longitudinally polarized vectors are equivalent to their corresponding
181 Goldstone scalars. The scattering amplitude can therefore be calculated with Goldstone diagrams.
182 In the so-called equivalent gauge [15], the Higgs doublet is then parametrized as:

$$H = \begin{pmatrix} i\pi_+ \\ \frac{\hat{h} + h - i\pi_0}{\sqrt{2}} \end{pmatrix}, \quad (2.22)$$

2.2 Heavy Vector Triplet

and the Goldstones π_0 and π_+ describe respectively W and Z longitudinal bosons; h is the physical Higgs boson. Rewriting the simplified Lagrangian 2.3 with 2.22 parametrization, two terms hold the information of the interaction of the V s with the Goldstones:

$$\mathcal{L}_\pi = \dots + c_H \zeta \hat{m}_V V_\mu^a \partial^\mu \pi^a + \frac{g_V c_H}{2} V_\mu^a (\partial^\mu h \pi^a - h \partial^\mu \pi^a + \epsilon^{abc} \pi^b \partial^\mu \pi^c) + \dots, \quad (2.23)$$

that are ruled by the $c_H g_V$ parameters combination. When ζ parameter is $\zeta \approx 1$, the first term in eq. 2.23 becomes important, and it is absorbed by a redefinition of the V_μ^a and π^a fields,

$$\begin{aligned} V_\mu^a &\rightarrow V_\mu^a + \frac{c_H \zeta}{\hat{m}_V} \partial_\mu \pi^a \\ \pi^a &\rightarrow \frac{1}{\sqrt{1 - c_H^2 \zeta^2}} \pi^a; \quad c_H^2 \zeta^2 < 1 \end{aligned} \quad (2.24)$$

By properly taking into account all the terms of the simplified lagrangian in the equivalent gauge, the partial widths of the dibosonic decays are ($\hat{m}_V = M_V$):

$$\begin{aligned} \Gamma_{V^0 \rightarrow W_L^+ W_L^-} &\approx \Gamma_{V^\pm \rightarrow W_L^\pm Z_L} \approx \frac{g_V^2 c_H^2 M_V}{192\pi} \frac{(1 + c_H c_{VVV} \zeta^2)^2}{(1 - c_H^2 \zeta^2)^2} = \frac{g_V^2 c_H^2 M_V}{192\pi} (1 + \mathcal{O}(\zeta^2)) \\ \Gamma_{V^0 \rightarrow Z_L h} &\approx \Gamma_{V^\pm \rightarrow W_L^\pm h} \approx \frac{g_V^2 c_H^2 M_V}{192\pi} \frac{(1 - 4 c_H c_{VVV} \zeta^2)^2}{(1 - c_H^2 \zeta^2)^2} = \frac{g_V^2 c_H^2 M_V}{192\pi} (1 + \mathcal{O}(\zeta^2)). \end{aligned} \quad (2.25)$$

2.2.2.3 Decays in fermions and bosons: concluding remarks

From eq. 2.21-2.25, some important conclusions can be extracted.

- When ζ parameter is small, all the triplet decays (both in fermions and in dibosons), branching fractions and productions are completely determined by $g^2 c_F/g_V$, $g_V c_H$, and the degenerate mass of the triplet M_V ,
- c_{VVV} , c_{VVHH} , c_{VWW} can be neglected, as long as the interest is focused in narrow resonances.

2.2.3 HVT production

Given the mass scale of the resonances, the production mechanisms expected to be relevant are Drell-Yan (fig. 2.1) and Vector Boson Fusion (VBF) (fig. 2.2).

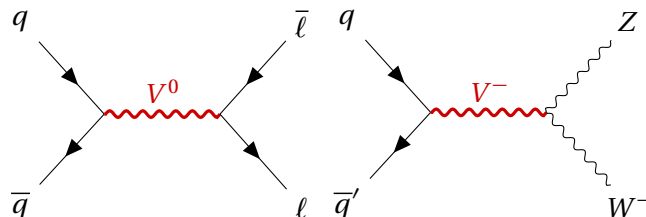


Figure 2.1: Examples of Drell-Yan production mechanism of a heavy V HVT boson: $q - \bar{q}$ quark scattering producing a neutral V^0 that decays leptonically (left); $q - \bar{q}'$ scattering producing a charged V^- that decays in a W and Z bosons (right).

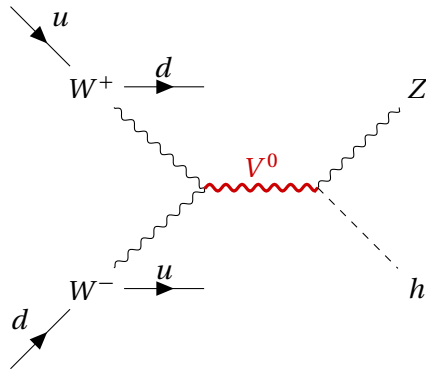


Figure 2.2: Example of VBF production mechanism of a heavy V HVT boson: a neutral V^0 boson is produced by a couple of W bosons, as a result of electroweak interactions of initial state u and d quarks. V^0 decays in a Z boson and a Higgs boson. The final state signature includes the presence of a pair of quarks, due to the primary interactions.

199 The cross-section of the production mechanisms is given by:

$$\sigma(pp \rightarrow V + X) = \sum_{i,j \in p} \frac{\Gamma_{V \rightarrow ij}}{M_V} f(J, S_i, S_j) g(C_i, C_j) \left. \frac{dL_{ij}}{ds} \right|_{s=M_V^2}, \quad (2.26)$$

200 where i, j are the partons involved in the hard interaction, Γ_{ij} is the partial width of the process
 201 $V \rightarrow ij$, $f(J, S_i, S_j)$ is a function of the spin of the resonance and of the partons, $g(C_i, C_j)$ is a func-
 202 tion of the colour factors of each parton, s is the center-of-mass energy and $\frac{dL_{ij}}{ds}$ are the parton
 203 luminosities, that are independent from HVT model (that enters only in Γ_{ij}).

204 Parton luminosities, calculated for a center-of-mass energy of 14 TeV starting from quark and anti-
 205 quark parton distribution functions (PDF), are displayed in fig. 2.3 (Drell-Yan mechanism) and 2.4
 206 (VBF mechanism). VBF luminosities are suppressed by the α_{EW} factor, therefore the process is rel-
 evant only when the bosonic decays of the triplet are dominant (strongly coupled scenario).

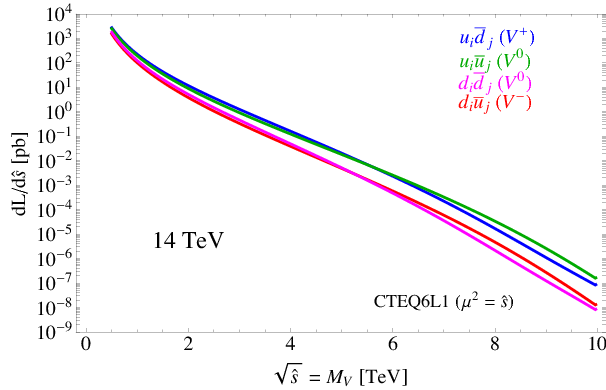


Figure 2.3: Parton luminosities for Drell-Yan process between i and j partons, as a function of the parton center-of-mass energy, for the LHC proton-proton collisions performed at 14 TeV.

2.2 Heavy Vector Triplet

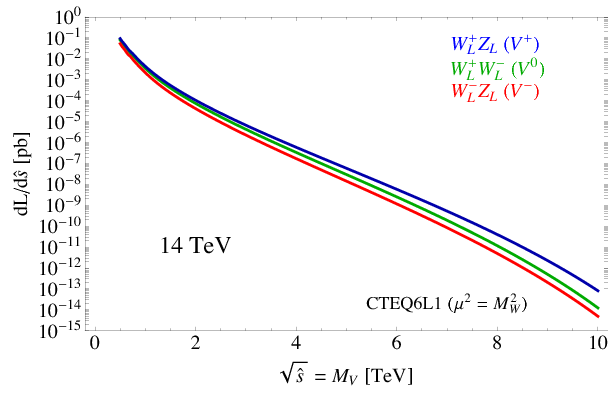


Figure 2.4: Parton luminosities for VBF process between i and j partons, as a function of the parton center-of-mass energy, for the LHC proton-proton collisions performed at 14 TeV.

2.2.4 Benchmark model A: weak coupling scenario

Model A scenario aims at reproducing a simple generalization of the SM [10], obtained by extending the gauge symmetry group with an additional $SU(2)'$. The low-energy phenomena are expected to be dominated by the SM, while the high-energy processes are relevant for the additional symmetry, bringing additional light vector bosons in play.

It can be shown that this kind of picture is portrayed by HVT when $c_H \sim -g^2/g_V^2$ and $c_F \sim 1$. This implies that:

$$\begin{aligned} g_V c_H &\approx g^2/g_V \\ g^2 c_F/g_V &\approx g^2/g_V, \end{aligned} \tag{2.27}$$

hence the partial decay widths into fermions (eq. 2.21) and bosons (eq. 2.25) differ only by a factor 2 and the colour factor (N_c). Branching fractions for the model A benchmark scenario ($g_V = 1$) are shown in fig. 2.5 (left); total widths are reported in fig. 2.5 (right) for different coupling parameters g_V .

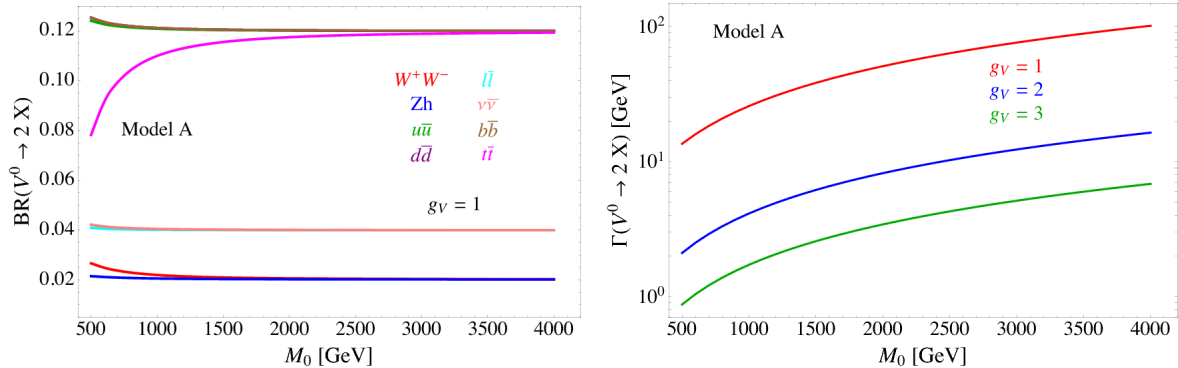


Figure 2.5: HVT model A scenario: branching fractions for fermionic and bosonic decays when $g_V = 1$ (left) as a function of the mass of the resonance M_0 ; total width of the resonance, as a function of its mass, considering different values of the parameter g_V (right).

219 **2.2.5 Benchmark model B: strong coupling scenario**

220 In composite Higgs models [12], the Higgs boson is the result of the spontaneous symmetry breaking
 221 of an $SO(5)$ symmetry to a $SO(4)$ group. New vector bosons are expected to appear, and the lightest
 222 ones can be represented by HVT model B when $c_H \sim c_F \sim 1$.

223 In this case:

$$g_V c_H \approx -g_V \\ g^2 c_F / g_V \approx g^2 / g_V, \quad (2.28)$$

224 hence the decay into bosons is not suppressed by g_V parameter. In the benchmark scenario $g_V = 3$,
 225 decays into dibosons are largely dominant, as it can be seen in fig. 2.6 (left); the total decay width
 226 increases for larger g_V (fig. 2.6, right). When the resonances start to be very broad, *i.e.* $\Gamma/M_V \gg$
 227 0.1, the assumptions leading to the simplified model are no longer valid, hence higher order, non-
 228 resonant effects must be taken into account.

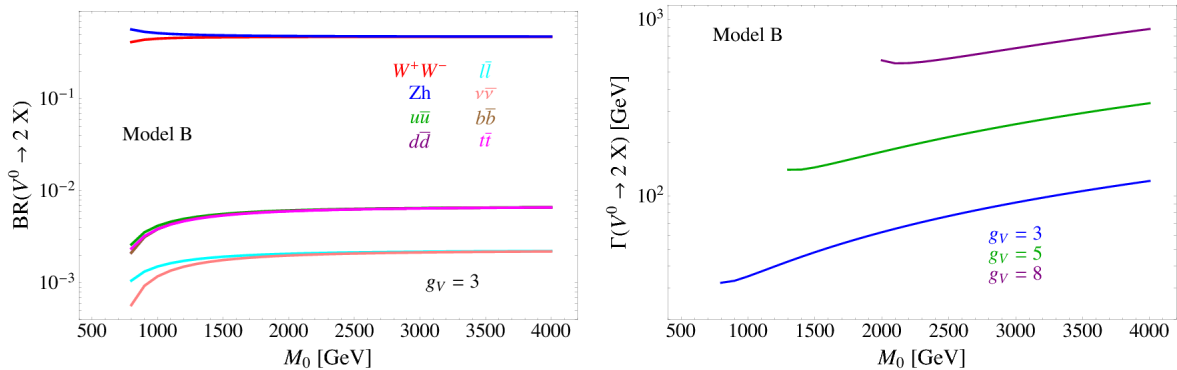


Figure 2.6: HVT model B scenario: branching fractions for fermionic and bosonic decays when $g_V = 3$ (left) as a function of the mass of the resonance M_0 ; total width of the resonance, as a function of its mass, considering different values of the parameter g_V (right).

229 **2.2.6 Search for HVT resonances at LHC**

230 No evidence of HVT resonances has been observed so far at LHC experiments. Data collected by
 231 ATLAS and CMS detectors are used to set limits on the HVT resonance masses and coupling param-
 232 eters. Experimental results from proton-proton collisions performed at a center-of-mass energy of
 233 8 TeV (Run 1 era) at LHC brought to the following conclusions. A weakly coupled resonance, in the
 234 context of benchmark model A ($g_V = 1$) was excluded up to 3 TeV by Run 1 data. By looking at parton
 235 luminosities in fig.2.3, in data produced by LHC proton-proton collision at 14 TeV, collected for an
 236 integrated luminosity of 300 fb^{-1} , the sensitivity is expected to increase up to $m_V \approx 6 \text{ TeV}$. A strongly
 237 coupled resonance, in the context of benchmark model B ($g_V = 3$) is excluded up to 2 TeV by Run 1
 238 data. Data produced by LHC at 14 TeV should increase the sensitivity up to $m_V \approx 3 - 4 \text{ TeV}$.
 239 The most stringent limits are provided by the latest data produced by LHC at a center-of-mass en-
 240 ergy of 13 TeV (Run 2 era).

241 Numerous searches for HVT triplet have been performed at CMS experiment in different final
 242 states: the most sensitive ones were those in all-hadronic topology. [16, 17] (search for WW , WZ ,
 243 ZZ resonances in the $q\bar{q}q\bar{q}$ final state) excludes a W' with mass below 3.6 and a Z' with mass below

2.2 Heavy Vector Triplet

244 2.7 TeV in the model B scenario (fig. 2.7). [18, 19] (search for WH , ZH resonances in the $q\bar{q}b\bar{b}$ final
 245 state) excludes a W' lighter than 2.97 (3.15) TeV in the HVT model A (model B), and a Z' up to 1.67
 246 (2.26) TeV in HVT model A (model B) (fig. 2.8). In fig. 2.9, results of [16, 17] (left) and [18, 19] (right)
 247 searches are interpreted as exclusion contours in the coupling parameter plane of the HVT model
 248 ($g_V c_H$ and $g^2 c_F/g_V$). In the grey shaded area, the narrow width approximation fails. The colored
 249 curves display the parameter exclusion for different mass hypotheses of the triplet. Colored dots
 250 show the model A and B benchmark scenarios.

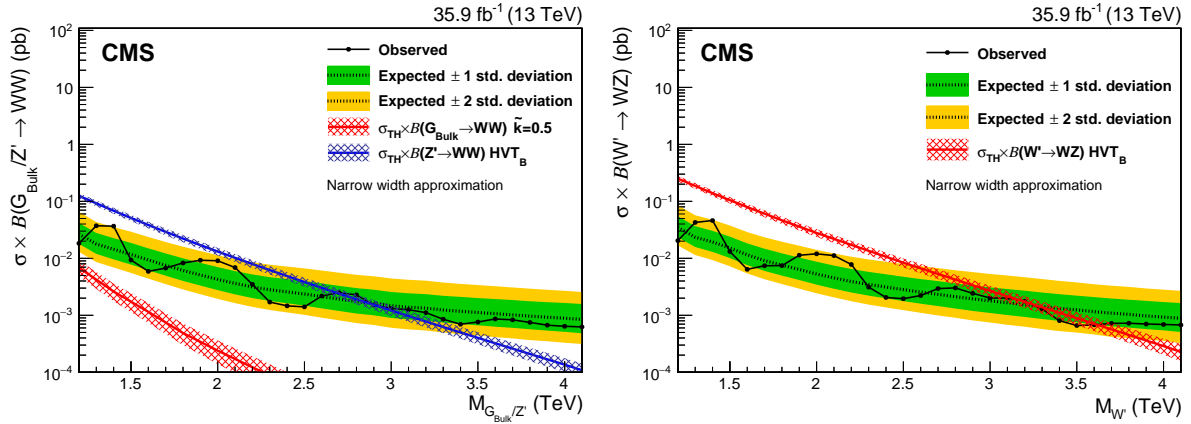


Figure 2.7: The observed and expected limits, with 68% and 95% uncertainty bands, on the product of the cross section and branching fraction $\sigma \mathcal{B}(Z' \rightarrow WW)$ for a spin-1 Z' (left) and $\sigma \mathcal{B}(W' \rightarrow WZ)$ for a spin-1 W' (right), as a function of the reconstructed mass of the diboson resonance. The colored lines show the theoretical predictions for the HVT model B.

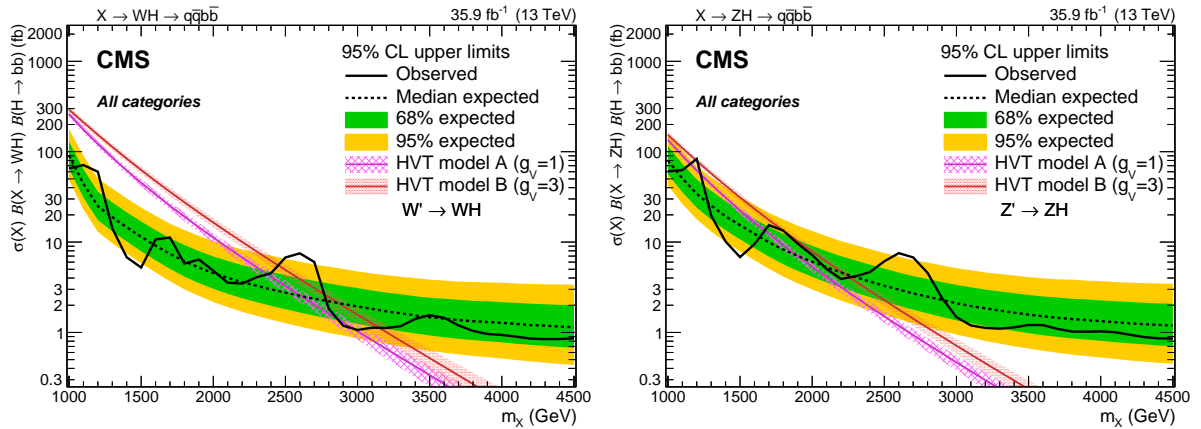


Figure 2.8: The observed and expected limits, with 68% and 95% uncertainty bands, on the product of the cross section and branching fraction $\sigma \mathcal{B}(W' \rightarrow WH)$ for a spin-1 W' (left) and $\sigma \mathcal{B}(Z' \rightarrow ZH)$ for a spin-1 Z' (right), as a function of the reconstructed mass of the diboson resonance. The colored lines show the theoretical predictions for the HVT model A and B.

251 Many other final states have been exploited at CMS: $ZW, ZZ \rightarrow \ell\bar{\ell}q\bar{q}$ [20]; $WH, ZH \rightarrow (\ell\bar{\ell}, \ell\nu, \nu\bar{\nu})b\bar{b}$ [21];
 252 $WZ, WW \rightarrow \ell\nu q\bar{q}$ [22]. Finally, $ZW, ZZ \rightarrow \nu\bar{\nu}q\bar{q}$ [23] results will be extensively described in this
 253 thesis.

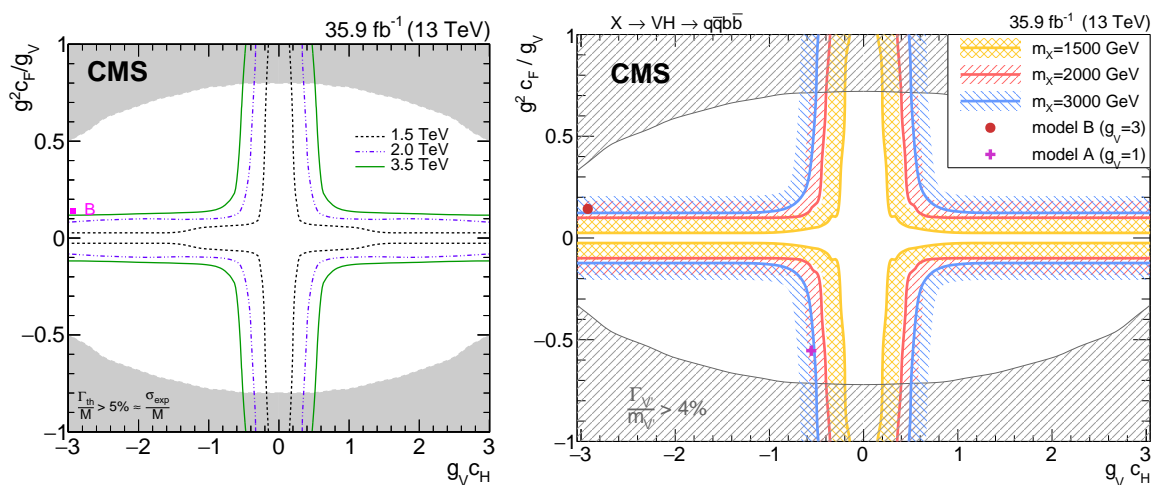


Figure 2.9: Exclusion contours in the coupling parameter plane of the HVT model ($g_V c_H$ and $g^2 c_F / g_V$).

2.2 Heavy Vector Triplet

254 Searches for HVT model B resonances have been performed at ATLAS experiment as well. Re-
 255 sults for a $W' \rightarrow WZ$ reported in fig. 2.10 include the searches performed in $WW, WZ, ZZ \rightarrow q\bar{q}q\bar{q}$
 256 final state [24]; $WZ, WW \rightarrow \ell\nu q\bar{q}$ final state [25]; $ZW, ZZ \rightarrow (\ell\bar{\ell}, \ell\nu, \nu\bar{\nu})q\bar{q}$ final state [26]. The all-
 257 hadronic final state has the best sensitivity and it excludes a W' resonance up to 3.3 TeV (model B
 258 scenario). Results for a $W' \rightarrow WH$ and for a $Z' \rightarrow ZH$ are displayed in fig. 2.11 (left and right respec-
 259 tively), and they include searches performed in $WH, ZH \rightarrow q\bar{q}b\bar{b}$ final state [27], and $WH, ZH \rightarrow$
 260 $\ell\bar{\ell}, \ell\nu, \nu\bar{\nu} b\bar{b}$ [28]. A W' is excluded up to 2.9 TeV and a Z' is excluded up to 2.8 TeV (in the model B
 261 scenario).

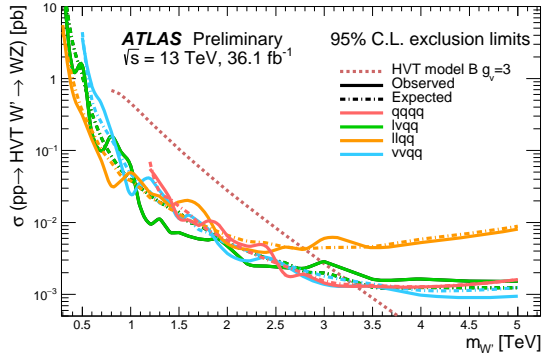


Figure 2.10: The observed and expected limits on the product of the cross section and branching fraction $\sigma \mathcal{B}(W' \rightarrow WZ)$ for a spin-1 W' , as a function of the reconstructed mass of the diboson resonance. The dotted line shows the theoretical predictions for the HVT model B.

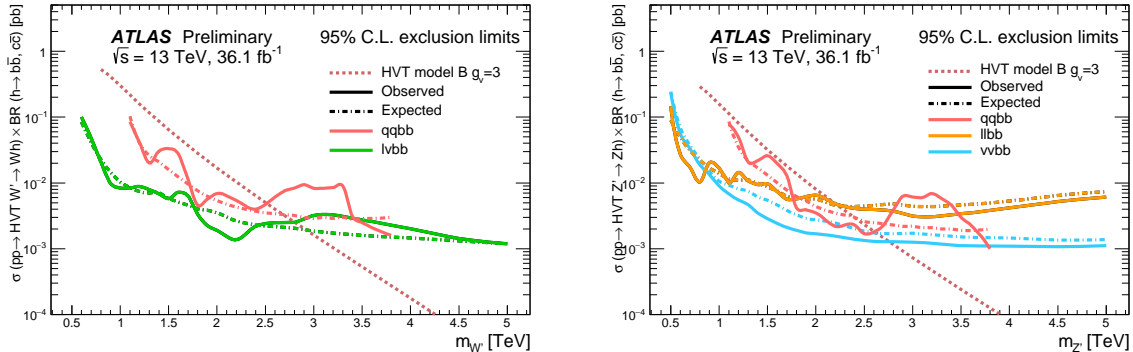


Figure 2.11: The observed and expected limits on the product of the cross section and branching fraction $\sigma \mathcal{B}(W' \rightarrow WH)$ for a spin-1 W' (left) and $\sigma \mathcal{B}(Z' \rightarrow ZH)$ for a spin-1 Z' (right), as a function of the reconstructed mass of the diboson resonance. The colored lines show the theoretical predictions for the HVT model B.

²⁶² **2.3 Warped extra dimension**

²⁶³ The Randall-Sundrum model [29, 30] (RS1) proposes the introduction of one additional warped di-
 264 mension in order to solve the hierarchy problem. The metric of the 5-dimensional space (a slice of
 265 AdS_5) generates an exponential hierarchy between the electroweak and Planck scales, associated re-
 266 spectively to the TeV three-brane, where the SM particles are confined, and the Planck three-brane.
 267 As a consequence of the new geometry, spin-2 massive gravitons are predicted to exist.
 268 The bulk extension of the Randall-Sundrum model [31, 32] states that the SM fields can propagate in
 269 the extra dimension. Light fermions are near the Planck brane, heavy fermions are close to the TeV
 270 brane, while the Higgs sector is confined in the TeV brane. Higgs couplings to the heavy fermions
 271 are therefore expected to be stronger: this naturally arising hierarchy of the masses of the SM fields
 272 gives a solution to the flavour problem. In this scenario, the fermionic decays of the bulk gravitons
 273 are suppressed, while the bosonic decays are preferred.

²⁷⁴ **2.3.1 Randall-Sundrum original model (RS1)**

²⁷⁵ The existence of additional n -dimensions implies that the effective Planck scale observed in 4-
 276 dimensions, $M_{PL} = 1.220910^{19}$ GeV, is related to the fundamental $4+n$ -dimensional Planck scale,
 277 M , via the geometry. M is expected to be of the order of the reduced $\overline{M}_{PL} = M_{PL}/2\pi$. If the 4-
 278 dimensional and the n additional metrics are factorizable, \overline{M}_{PL} is the product of M and the volume
 279 of the compact space V_n :

$$\overline{M}_{PL}^2 = V_n M^{2+n}. \quad (2.29)$$

²⁸⁰ If $M \sim$ TeV, this implies that V_n must be very large, hence the compactification scale $\mu \sim 1/V_n^{1/n}$
 281 is small (eV – MeV for $n=2 - 7$). Given the smallness of μ when compared to the electroweak scale,
 282 the effects of the extra dimensions should be evident in SM processes. Since they are not observed,
 283 SM particles are assumed to be confined in a 4-dimensional space, the TeV three-brane, while only
 284 gravity is allowed to propagate into the $4+n$ -dimensional space, the bulk. This mechanism solves
 285 the hierarchy of the Higgs scale but introduces a new hierarchy between μ and M .
 286 In the Randall-Sundrum model [29, 30], only one additional dimension is added. The geometry of
 287 the 5-dimensional bulk is non-factorizable, and it is a slice of AdS_5 spacetime.¹ The 4-dimensional
 288 metric is multiplied by an exponential function of the fifth dimension (the "warp" factor):

$$ds^2 = e^{-2kr_c\phi} \eta_{\mu\nu} dx^\mu dx^\nu + r_c^2 d\phi^2; \quad (2.30)$$

²⁸⁹ x^μ are the usual 4-dimensional coordinates, $\eta_{\mu\nu} = diag(-1, 1, 1, 1)$ is the Minkowski metric, k is a
 290 scale of order of \overline{M}_{PL} , ϕ is the coordinate of the extra dimension, $0 < |\phi| < \pi$, and r_c is the com-
 291 pactification radius of this finite interval. 4-dimensional mass scales are obtained by multiplying
 292 the bulk masses by $e^{-2kr_c\phi}$: given the exponential form of the warp factor, a small r_c suffices for
 293 generating a large hierarchy between Planck and Higgs scales.

²⁹⁴ Two 4-dimensional three-branes are located at the boundaries of the fifth dimension: the visible
 295 brane at $\phi = \pi$; the hidden brane at $\phi = 0$, and their metrics are obtained starting from the bulk
 296 5-dimensional metric G_{MN} , where $M, N = \mu, \phi$:

$$\begin{aligned} g_{\mu\nu}^{\text{vis}}(x^\mu) &= G_{\mu\nu}(x^\mu, \phi = \pi) \\ g_{\mu\nu}^{\text{hid}}(x^\mu) &= G_{\mu\nu}(x^\mu, \phi = 0). \end{aligned} \quad (2.31)$$

¹An n -dimensional anti-de Sitter space (AdS_n) is a maximally symmetric Lorentz manifold, that solves the Einstein equation with a negative curvature (negative cosmological constant).

2.3 Warped extra dimension

297 The classical action is given by:

$$\begin{aligned} S &= S_{\text{gravity}} + S_{\text{vis}} + S_{\text{hid}} \\ S_{\text{gravity}} &= \int d^4x \int_{-\pi}^{+\pi} d\phi \sqrt{-G} (-\Lambda + 2M^3 \mathcal{R}) \\ S_{\text{vis}} &= \int d^4x \sqrt{-g_{\text{vis}}} (\mathcal{L}_{\text{vis}} - V_{\text{vis}}) \\ S_{\text{hid}} &= \int d^4x \sqrt{-g_{\text{hid}}} (\mathcal{L}_{\text{hid}} - V_{\text{hid}}), \end{aligned} \quad (2.32)$$

298 where G (g) is the trace of the G_{MN} ($g_{\mu\nu}$) metric, Λ is the cosmological constant in the bulk, \mathcal{R} is
299 the 5-dimensional Ricci scalar, \mathcal{L} and V are the lagrangian and the vacuum energy of the hidden
300 and visible branes.

301 A 5-dimensional metric that preserves the 4-dimensional Poincaré invariance has the form:

$$ds^2 = e^{-2\sigma(\phi)} \eta_{\mu\nu} dx^\mu dx^\nu + r_c^2 d\phi^2. \quad (2.33)$$

302 The Poincaré invariance guarantees that r_c does not depend on x^μ . Given 2.33, the solution of the
303 5-dimensional Einstein's equations simplifies into:

$$\sigma = r_c |\phi| \sqrt{\frac{-\Lambda}{24M^3}}. \quad (2.34)$$

304 Furthermore, the Poincaré invariance imposes constraints to the vacuum energies and cosmologi-
305 cal constant:

$$\begin{aligned} V_{\text{hid}} &= -V_{\text{vis}} = 24M^3 k \\ \Lambda &= -24M^3 k^2. \end{aligned} \quad (2.35)$$

306 The final 5-dimensional metric is then:

$$ds^2 = e^{-2kr_c|\phi|} \eta_{\mu\nu} dx^\mu dx^\nu + r_c^2 d\phi^2. \quad (2.36)$$

307 A small r_c is considered, so the effects of the fifth dimension on 4-dimensional spacetime can't
308 be appreciated. A 4-dimensional effective field theory approach is therefore motivated, and its mass
309 parameters are related to the bulk parameters, M , k and r_c . In the Randall-Sundrum model, SM
310 matter fields are confined in the TeV brane.

311 The massless gravitons, the mediators of the gravitational interaction in the effective field theory, are
312 the zero modes ($h_{\mu\nu}$) of the quantum fluctuations of the classical solution (2.36):

$$ds^2 = e^{-2kT(x)|\phi|} (\eta_{\mu\nu} + h_{\mu\nu}(x)) dx^\mu dx^\nu + T^2(x) d\phi^2, \quad (2.37)$$

313 where the usual Minkowski metric has been replaced by $\bar{g}_{\mu\nu}(x) = \eta_{\mu\nu} + h_{\mu\nu}$; $h_{\mu\nu}$ are the tensor fluc-
314 tuations around the Minkowski space, and represent both the physical graviton in 4-dimensions
315 and the massless mode of the Kaluza-Klein decomposition of the bulk metric. r_c is the vacuum ex-
316 pectation value of $T(x)$.

317 By substituting eq. 2.37 in the classical action 2.32, an effective action can be extracted, and in par-
318 ticular the curvature term holds:

$$S_{\text{eff}} \sim \int d^4x \int_{-\pi}^{+\pi} d\phi 2M^3 r_c e^{-2kr_c|\phi|} \bar{\mathcal{R}} \sqrt{-\bar{g}}, \quad (2.38)$$

319 where \bar{g} is the trace of $\bar{g}_{\mu\nu}$ and $\bar{\mathcal{R}}$ is the 4-dimensional Ricci scalar of $\bar{g}_{\mu\nu}$ metric. In this effective
 320 4-dimensional action, the ϕ dependence can be integrated out, and the 4-dimensional Planck mass
 321 can be calculated:

$$\bar{M}_{PL}^2 = M^3 r_c \int_{-\pi}^{+\pi} d\phi e^{-2kr_c|\phi|} = \frac{M^3}{k} (1 - e^{-2kr_c\pi}). \quad (2.39)$$

322 It can be shown [29] that a field with a fundamental mass parameter m_0 in the bulk manifests in the
 323 visible three-brane with a physical mass m :

$$m = e^{-2kr_c\pi} m_0. \quad (2.40)$$

324 Scales $m \sim \text{TeV}$ are generated from $m_0 \sim \bar{M}_{PL}$ if $e^{kr_c\pi} \sim 10^{15}$. This relation stands still when Higgs
 325 field is introduced and confined in the visible three-brane:

$$v = e^{-2kr_c\pi} v_0, \quad (2.41)$$

326 where v is the Higgs vacuum expectation value in the TeV brane and v_0 is the 5-dimensional Higgs
 327 v.e.v.

328 The hierarchy problem is then solved by the exponential warp factor. The weakness of gravity in the
 329 TeV three-brane is motivated by the small overlap of the graviton wave function.

330 In order to calculate the mass spectrum of the graviton in the TeV brane, the tensor fluctuations of
 331 the Minkowski metric are expanded into a Kaluza-Klein (KK) tower $h_{\mu\nu}^{(n)}$:

$$h_{\mu\nu}(x, \phi) = \sum_{n=0}^{\infty} h_{\mu\nu}^{(n)}(x) \frac{\chi^{(n)}(\phi)}{\sqrt{r_c}}. \quad (2.42)$$

332 Once a suitable gauge is chosen, i.e. $\eta^{\mu\nu} \partial_\mu h_{\nu a}^{(n)} = \eta^{\mu\nu} h_{\mu\nu}^{(n)} = 0$, the equation of motion of $h_{\mu\nu}^{(n)}$ becomes
 333 the Klein-Gordon relation, where $m_n^G \geq 0$:

$$(\eta^{\mu\nu} \partial_\mu \partial_\nu - (m_n^G)^2) h_{\mu\nu}^{(n)}(x) = 0. \quad (2.43)$$

334 By substituting eq. 2.42 into Einstein's equation, the solutions for $\chi^{(n)}(\phi)$ (commonly called "pro-
 335 files") are [33, 34]:

$$\chi^{(n)}(\phi) = \frac{e^{2\sigma}}{N} [J_2(z_n^G) + \alpha_n Y_2(z_n^G)], \quad (2.44)$$

336 where J_2 and Y_2 are second order Bessel functions, N is the normalization of the wavefunction, α_n
 337 are coefficients and $z_n^G = m_n^G e^{\sigma(\phi)}/k$. m_n^G is the mass of the n -mode, and it depends on the roots
 338 of the Bessel functions $z_n^G = (3.83, 7.02, 10.17, 13.32, \dots)$. In the limit $m_n^G/k \ll 1$ and $e^{kr_c\pi} \gg 1$:

$$m_n^G = k z_n^G(\pi) e^{-kr_c\pi}. \quad (2.45)$$

339 The interactions between the graviton KK modes and the matter fields in the TeV brane can be de-
 340 rived from the 4-dimensional effective Lagrangian, once $h_{\mu\nu}$ is replaced by its KK decomposition:

$$\mathcal{L} = -\frac{1}{\bar{M}_{PL}} T^{\mu\nu}(x) h_{\mu\nu}^{(0)} - \frac{1}{e^{-kr_c\pi} \bar{M}_{PL}} T^{\mu\nu}(x) \sum_{n=1}^{\infty} h_{\mu\nu}^{(n)}(x); \quad (2.46)$$

342 $T^{\mu\nu}$ is the space energy-momentum tensor of the matter fields. The zero mode of the gravitons cou-
 343 pling is $1/\bar{M}_{PL}$, while higher order KK modes couplings to all SM fields are suppressed by $e^{-kr_c\pi} \bar{M}_{PL}$,
 344 that is of the order of the TeV scale. Spin-2 KK masses and couplings are hence determined by the
 345 TeV scale, or, equivalently, KK gravitons are close to the TeV brane. This implies that KK gravitons
 346 can be produced via $q\bar{q}$ or gluon fusion, and that a leptonic decay of the resonance could represent
 347 a very clear signal signature.

2.3 Warped extra dimension

2.3.2 Bulk extension of RS1: graviton production and decays

An extension of the original RS1 formulation has been proposed. It states that the usual SM fields are no longer confined in the TeV brane, but they are the zero modes of the corresponding 5-dimensional SM fields. If first and second generation fermions are close to the Planck brane, contribution to flavour changing neutral currents by higher-dimensional operators are suppressed. These contributions are excluded by electroweak precision tests, but they were not prevented in original RS1. The second motivation behind the choice is, as mentioned previously, the naturally arising flavour hierarchy: first and second generation quarks have small Yukawa couplings to the Higgs sector, confined in the TeV brane, while top quark and bosons have stronger Yukawa couplings.

In this picture, couplings between higher-order KK gravitons and light fermions are strongly suppressed, resulting into a negligible KK gravitons production via $q\bar{q}$, whilst gluon fusion production becomes dominant. KK gravitons decay into top quarks and Higgs bosons are dominant, given that both their profiles are near the TeV brane, while leptonic decays are negligible. Via the equivalence theorem, the Goldstone bosons are equivalent to the longitudinally polarized weak bosons, W_L^\pm and Z_L , that have profiles close to the TeV brane. Decays of KK gravitons into weak dibosons (and production in VBF) are comparable to di-top and di-Higgs decays.

The KK decomposition and the KK mass spectrum of the graviton have already been presented in sec. 2.3.1. The KK decomposition of a massless 5-dimensional gauge field $A_M(x, \phi)$ is similarly performed [35]:

$$A_\mu(x, \phi) = \sum_{n=0}^{\infty} A_\mu^{(n)}(x) \frac{\chi^{(n)_A}(\phi)}{\sqrt{r_c}}. \quad (2.47)$$

The profiles for the gauge fields are:

$$\chi_A^{(n)}(\phi) = \frac{e^\sigma}{N_A} [J_1(z_n^A) + \alpha_n^A Y_1(z_n^A)], \quad (2.48)$$

where J_1 and Y_1 are first order Bessel functions. Similarly to eq. 2.49, the mass spectrum of the gauge field is:

$$m_n^A = k z_n^A(\pi) e^{-k r_c \pi}; \quad (2.49)$$

the first roots of the Bessel functions are $z_n^A = (2.45, 5.57, 8.70, 11.84, \dots)$.

The Lagrangian expressing the interaction between the m and n modes of the bulk field F to the q KK gravitons mode G is [35]:

$$\mathcal{L}_{G-F} = \sum_{m,n,q} C_{mnq}^{FFG} \frac{1}{M_{PL}} \eta^{\mu\alpha} \eta^{\nu\beta} h_{\alpha\beta}^{(q)}(x) T_{\mu\nu}^{(m,n)}(x), \quad (2.50)$$

C_{mnq}^{FFG} is the overlap integral of the profiles:

$$C_{mnq}^{FFG} = \int \frac{d\phi}{\sqrt{k}} e^{t\sigma} \frac{\chi_F^{(m)} \chi_F^{(n)} \chi_G^{(q)}}{\sqrt{r_c}}; \quad (2.51)$$

t depends on the type of field considered.

The coupling between gluons and the q KK graviton mode is given by:

$$C_{00q}^{AAG} = e^{k\pi r_c} \frac{2[1 - J_0(x_n^G)]}{k\pi r_c (x_n^G)^2 |J_2(x_n^G)|}. \quad (2.52)$$

³⁷⁷ Once eq. 2.52 is put in eq. 2.50, the most significant partial decay widths into the q KK graviton mode
³⁷⁸ are:

$$\begin{aligned}\Gamma(G \rightarrow t_R \bar{t}_R) &\sim N_c \frac{\left[\tilde{k} x_q^G\right]^2 m_q^G}{320\pi} \\ \Gamma(G \rightarrow hh) &\sim \frac{\left[\tilde{k} x_q^G\right]^2 m_q^G}{960\pi} \\ \Gamma(G \rightarrow W_L^+ W_L^-) &\sim \frac{\left[\tilde{k} x_q^G\right]^2 m_q^G}{480\pi} \\ \Gamma(G \rightarrow Z_L Z_L) &\sim \frac{\left[\tilde{k} x_q^G\right]^2 m_q^G}{960\pi},\end{aligned}\tag{2.53}$$

³⁷⁹ where $\tilde{k} = k/\overline{M}_{PL}$; the total decay width is:

$$\Gamma_G = \frac{13 \left[\tilde{k} x_q^G\right]^2 m_q^G}{960\pi}.\tag{2.54}$$

³⁸⁰ Calculations, so far, have been performed considering $M \sim \overline{M}_{PL}$ and $k < M$, hypotheses under
³⁸¹ which the solution for the bulk metric (eq. 2.36) is valid. Hence, $\tilde{k} = k/\overline{M}_{PL} \leq 1$ is taken as a ref-
³⁸² erence interval. This has also phenomenological consequences on the width of the resonance, as
³⁸³ stated in eq. 2.54. The total decay width of the lightest KK graviton mode, compared to its mass,
³⁸⁴ is shown as a function of \tilde{k} in fig. 2.12 [36]. At $\tilde{k} = 1$, in the bulk scenario, the KK graviton width is
³⁸⁵ expected to be few % of its mass, up to 4 TeV (dotted red curve). The narrow width approximation
³⁸⁶ holds, hence the resonance properties can be probed at the peak, neglecting the effects in the tails
³⁸⁷ of the mass distribution.

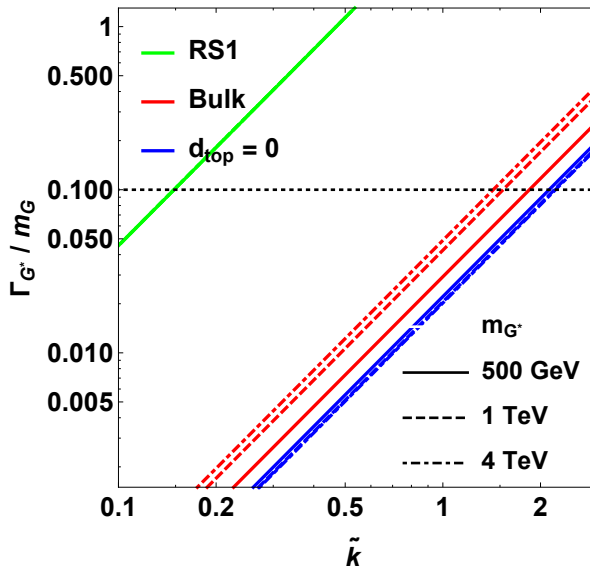


Figure 2.12: Width of the KK gravitons, in units of the mass of the resonance, as a function of the curvature parameter \tilde{k} . The red curves represent the bulk extension of RS1 original model for different mass hypotheses (from 500 GeV up to 4 TeV).

³⁸⁸ The total cross-section of a bulk graviton, produced at LHC in proton-proton interactions via
³⁸⁹ gluon fusion (displayed in fig. 2.13), decaying into a couple of vector bosons (for the purpose of this

2.3 Warped extra dimension

thesis, a final state with two longitudinally polarized Z bosons is considered) is expressed as a function of the parton level cross-section $\hat{\sigma}$, the gluon parton distribution functions f_g , the momentum transfer $Q^2 \sim (m_q^G)^2$ and the center-of-mass energy s :

$$\sigma(pp \rightarrow ZZ) = \int dx_1 dx_2 f_g(x_1, Q^2) f_g(x_2, Q^2) \hat{\sigma}(x_1 x_2 s). \quad (2.55)$$

The differential parton level cross-section, averaged over colors and initial spin states, is (hatted quantities are calculated in the center-of-mass frame):

$$\frac{d\hat{\sigma}(gg \rightarrow ZZ)}{d \cos \hat{\theta}} \approx \frac{|\mathcal{M}_{+00}|^2}{1024\pi \hat{s}}, \quad (2.56)$$

where $|\mathcal{M}_{+00}|$ is the matrix element of the dominant contribution in $gg \rightarrow VV$ process (Γ_G is defined in eq. 2.54, a, b are color factors):

$$\mathcal{M}_{+00}(g^a g^b \rightarrow VV) = -C_{00q}^{AAG} e^{-k\pi r_c} \left(\frac{x_n^G \tilde{k}}{m_n^G} \right)^2 \sum_n \frac{\delta_{ab} \mathcal{A}_{+00}}{\hat{s} - m_n^G + i\Gamma_G m_n^G}. \quad (2.57)$$

The relevant amplitudes taken account in the matrix element calculation are [31]:

$$\mathcal{A}_{+00} = \mathcal{A}_{-00} = \frac{(1 - 1/\beta_Z^2)(\beta_Z^2 - 2)[(\hat{t} - \hat{u})^2 - \beta_Z^2 \hat{s}^2]\hat{s}}{8M_Z^2}, \quad (2.58)$$

where $\beta_Z^2 = 1 - 4M_Z^2/\hat{s}$ and M_Z is the mass of the Z boson.

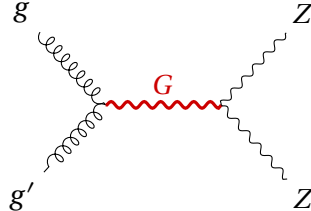


Figure 2.13: Gluon fusion production mechanism for a KK graviton that decays in a couple of Z bosons.

399 **2.3.3 Search for KK bulk gravitons at LHC**

400 No evidence of spin-2 bulk graviton resonances has been observed so far at LHC experiments. Data
 401 collected by ATLAS and CMS detectors are used to set limits on the graviton masses, generally con-
 402 sidering different curvature parameter \tilde{k} hypotheses, once assured the narrow width approximation
 403 is still valid (up to $\tilde{k} \sim 1$). The most stringent limits have been set with Run 2 data.

404 Many results of the diboson searches performed at CMS and already presented in sec. 2.2.6 are
 405 interpreted in the context of the bulk gravitons, together with the additional final states $WZ, ZZ \rightarrow$
 406 $\ell\bar{\ell}\nu\bar{\nu}$ [37] and $HH \rightarrow b\bar{b}b\bar{b}$ [38]. The most interesting limit is provided by [37], that, under the
 407 hypothesis $\tilde{k} = 0.5$, excludes a spin-2 bulk graviton with a mass lower than 800 GeV (fig. 2.14).

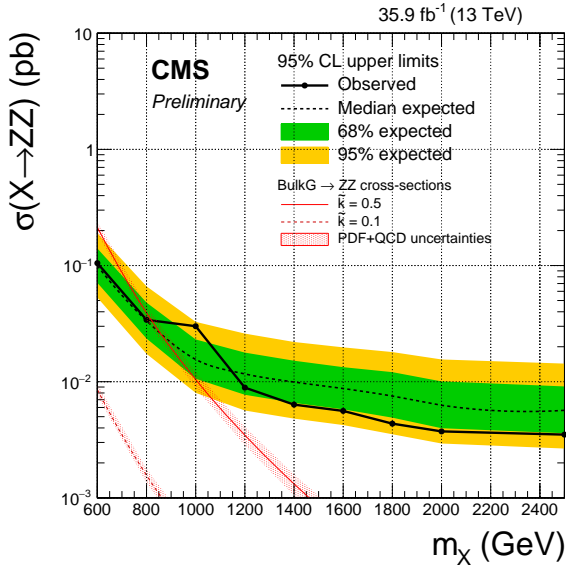


Figure 2.14: The observed and expected limits, with 68% and 95% uncertainty bands, on the product of the cross section and branching fraction $\sigma \mathcal{B}(G \rightarrow ZZ)$ for a spin-2 bulk graviton, as a function of the reconstructed mass of the diboson resonance. The colored lines show the theoretical predictions for $\tilde{k} = 0.1$ and 0.5 .

408 Similarly for ATLAS experiment, searches for diboson resonances in sec. 2.2.6 have been inter-
 409 preted in the graviton context. The most stringent limit is given by [25], where, under the assump-
 410 tion $\tilde{k} = 1$, a spin-2 bulk graviton with mass lower than 1.76 TeV is excluded (fig. 2.15).

2.3 Warped extra dimension

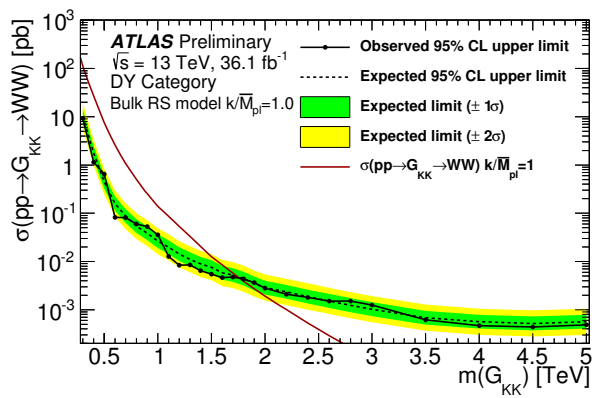


Figure 2.15: The observed and expected limits, with 68% and 95% uncertainty bands, on the product of the cross section and branching fraction $\sigma \mathcal{B}(G \rightarrow ZZ)$ for a spin-2 bulk graviton, as a function of the reconstructed mass of the diboson resonance. The colored lines show the theoretical predictions for $\tilde{k} = 1$.

The Large Hadron Collider and the CMS experiment

412

413

414 Brief intro to CERN and LHC

415 • research

416 • technology

417 • education

418 • collaboration

419

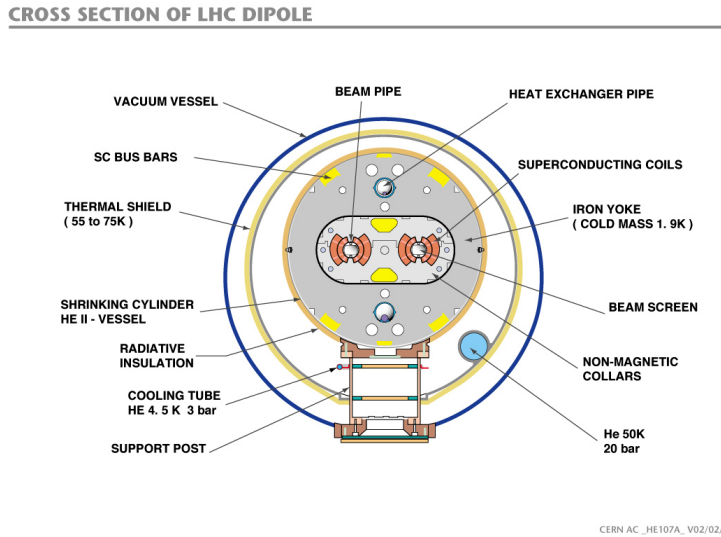
3.1 The Large Hadron Collider

420 The Large Hadron Collider (LHC) is a 27 km ring structure designed for the acceleration and collision
 421 of protons and heavy ions. It is situated approximately 100 m underground, between France and
 422 Switzerland, in the Geneva area, and it is the most important of the CERN (Conseil européen pour
 423 la recherche nucléaire) facilities. In order to reduce the cost of the project, definitively approved in
 424 1996, the LHC has been designed to fit the pre-existing underground tunnel of the Large Electron-
 425 Positron collider (LEP) [ref. 24 Jacopo], built to accelerate electrons and positrons and running until
 426 the year 2000.

427 Moving from an electron-positron collider to an hadron collider allowed to reach higher energies in
 428 the center-of-mass frame, since the synchrotron radiation loss is inversely proportional to the fourth
 429 power of the mass of the particle involved: hence, it is reduced by a factor $m_p/m_e \sim 10^3$. Furthermore,
 430 at a proton-proton collider it is possible to collect higher luminosities (and hence more
 431 statistics) with regards to, for example, a proton-antiproton collider, like Tevatron at Fermilab, in
 432 the USA.

433 In the LHC two identical beam pipes rings are designed to let protons circulate in opposite di-
 434 rections, in ultrahigh vacuum conditions (10^{-11} – 10^{-10} mbar) in order to avoid collisions with gas
 435 molecules. Given the reduced available diameter in the tunnel (4 m), the two proton beams are
 436 magnetically coupled. The collider is composed by 8 arc sections (48 km) driving protons around

437 the ring, and straight sections (6 km) where beam control systems and detectors are inserted. Pro-
 438 ton beams collide in four interaction points, where the four main LHC experiments are installed:
 439 ALICE, ATLAS, CMS, LHCb.



CERN AC _HE107A_ V02/02/98

Figure 3.1: Section of the LHC dipole magnet structure.

440 In fig. 3.1, a slice of the arc section is displayed. Around the beam pipes, two superconducting mag-
 441 netic dipoles are located: they generate vertical magnetic fields in opposite directions. The super-
 442 conducting coils are made of niobium-titanium, materials that are superconducting at very low
 443 temperature. At the LHC, they are kept at a temperature of 1.9 K (-271.3°C) by a closed liquid helium
 444 circuit. A current of 11850 A flows through the magnets, without any energy loss due to electrical
 445 resistance, generating a magnetic field of 8.33 T. Magnets of higher order in multipole expansion
 446 (quadrupoles, sextupoles, octupoles, ...) are used to optimize the proton trajectories; in particular,
 447 quadrupoles allow to focus and squeeze the beams. Along the LHC ring here are 9593 magnets; 1232
 448 are dipoles, 392 are quadrupoles.

449 The LHC represents the final step of the CERN accelerator complex, showed in fig. 3.2. Protons are
 450 extracted from hydrogen atoms and inserted in the linear accelerator Linac2, that brings them to an
 451 energy of 50 MeV. They circulate around a little synchrotron, Proton Synchrotron Booster, reaching
 452 an energy of 1.4 GeV, and then in the Proton Synchrotron (PS), where their energy is increased to 25
 453 GeV. The second to last step is the Super Proton Synchrotron, SPS, accelerating protons up to 450
 454 GeV. They are finally injected in the Large Hadron Collider, where sixteen radiofrequency cavities
 455 (RF) accelerate protons inside each beam up to an energy of 6.5 TeV, providing a center-of-mass en-
 456 ergy of 13 TeV when colliding. The RF cavities provide an accelerating electromagnetic field up to 5
 457 MV/m (maximum voltage of 2 MV), that oscillates with a frequency of 400 MHz. Like the magnets,
 458 the cavities are kept at low temperature (4.5 K, or -268.7°C) in order to allow superconducting con-
 459 ditions. The maximum beam energy can be reached in 15 minutes. After several hours of collisions
 460 (~ 10 hours), the quality of the beams deteriorates and they are extracted from the machine and
 461 dumped.

462
 463 Protons circulate inside the LHC ring in bunches of $\sim 10^{11}$ particles each, 80 mm long. Focusing
 464 magnets allow to reduce the bunch diameter down to 16 μm . Different bunches are separated by 25
 465 ns (or, ~ 7.5 m), corresponding to a frequency of 40 MHz and an instantaneous (peak) luminosity
 466 (defined in eq. 3.1) of $1.2 \times 10^{34} \text{ cm}^{-2}\text{s}^{-1}$. Given the structure of the beams, at every bunch crossing

3.1 The Large Hadron Collider

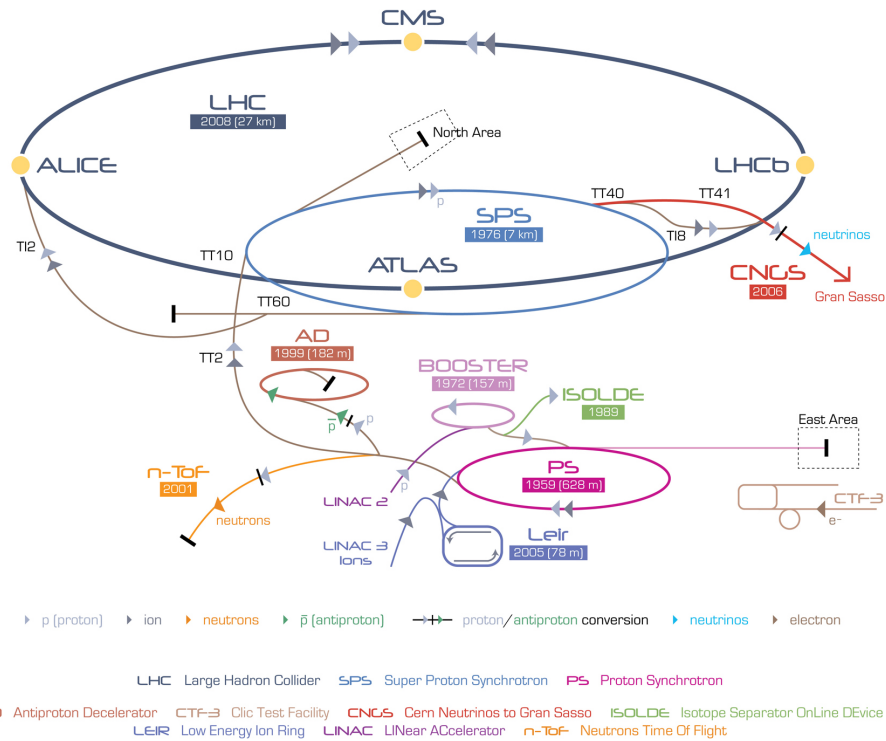


Figure 3.2: The CERN accelerator complex.

many protons interact simultaneously: this phenomenon is called pile-up. The designed maximum number of bunches is 2808.

The main parameters that describes an hadronic collider are the center-of-mass energy, corresponding to the sum of the energies of the beams, and the instantaneous luminosity, that describes the frequency of the interactions among the bunches in the beams. If the bunches in the first beam contain n_1 protons, and the bunches in the second beam contain n_2 protons, and if the colliding area is Σ , the frequency of complete turns around the ring is f , the instantaneous luminosity $\mathcal{L}_{\text{inst}}$ is:

$$\mathcal{L}_{\text{inst}} = f \frac{n_1 n_2}{\Sigma}. \quad (3.1)$$

If a generic physics process i has a cross-section of σ_i , the interaction rate R_i is:

$$R_i = \frac{dN_i}{dt} = \sigma_i \mathcal{L}_{\text{inst}}, \quad (3.2)$$

and the number of events recorded in the time interval $(0, \tau)$ is obtained by the integrated luminosity $\mathcal{L} = \int_0^\tau \mathcal{L}_{\text{inst}} dt$:

$$N_i = \sigma_i \int_0^\tau \mathcal{L}_{\text{inst}} dt. \quad (3.3)$$

In fig. 3.3, a summary of the luminosity measurement in 2016 data is presented. The luminosity delivered by LHC is represented in blue, the recorded by CMS is in orange. The mean number of interaction per bunch crossing (pile-up) is presented as well. The average number of interactions per collision is 27, the maximum is around 50.

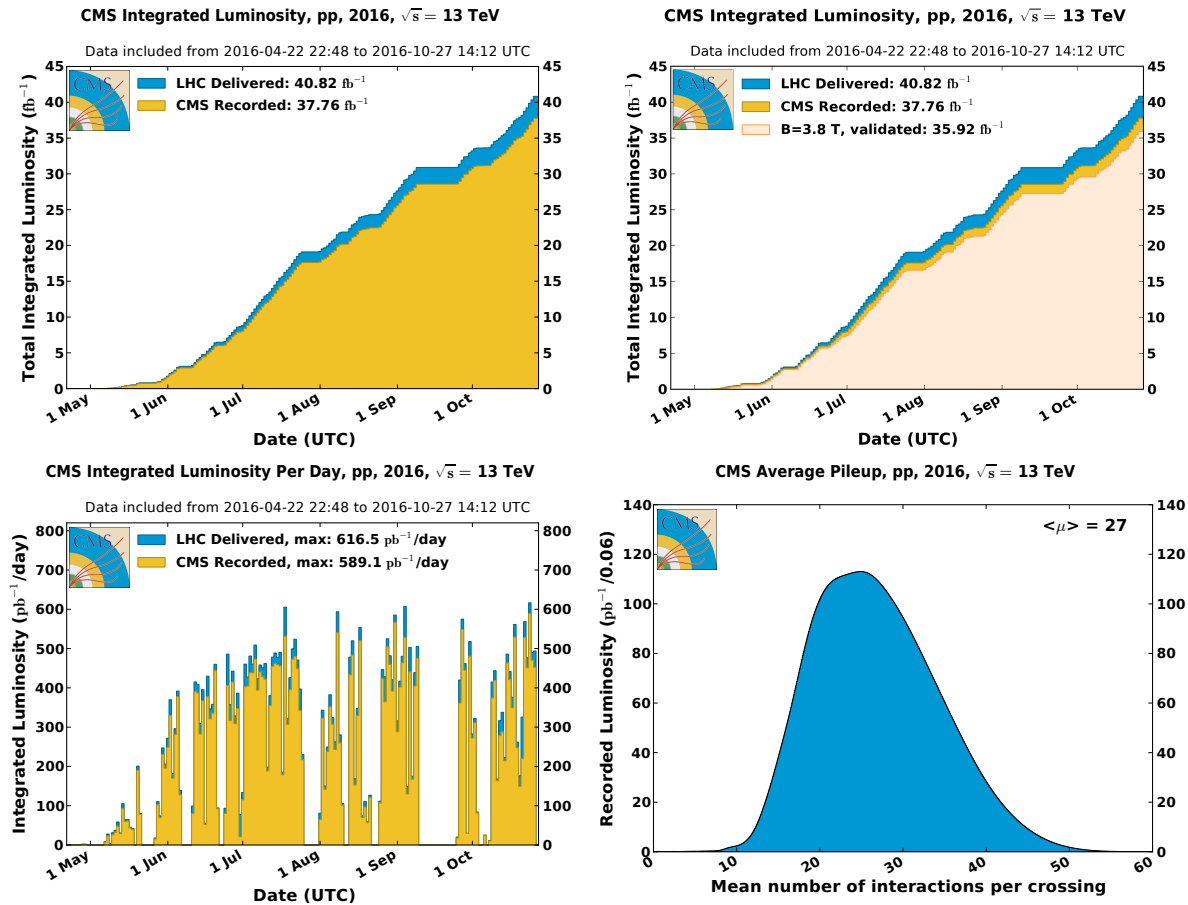


Figure 3.3: Luminosity in 2016 LHC data. Top-left plot: the cumulative integrated luminosity delivered by LHC (in blue) and recorded by CMS (in orange), as a function of the data taken period. Top-right plot: data recorded by CMS and declared as optimal for the physics analyses (in light orange), corresponding to a total integrated luminosity of 35.9 fb^{-1} . Bottom-left plot: maximum integrated luminosity per day. Bottom-right plot: number of proton interactions per bunch crossing (pile-up).

483 3.1.1 Proton-proton interactions

484 Proton-proton collisions allow to reach higher energies and luminosities, but the drawback is the
 485 complexity of the events when compared to electron-positron collisions: not only because of the in-
 486 creasing backgrounds due to strong interactions among partons, but also because the momenta of
 487 the proton partons taking part in the interaction are unknown; not to mention the problem of disen-
 488 tangling the tracks of the particles coming from the interesting hard interactions from the spectator
 489 pile-up interactions (in fig. 3.4, 78 proton collisions were happening at the same bunch crossing).
 490 The majority of the LHC events is represented by soft interactions, with low transverse momen-
 491 tum transfer, namely elastic and diffractive scatterings. In the so-called hard interactions, on the
 492 other hand, the transferred momentum among particles is high, allowing to produce massive reso-
 493 nant phenomena. These events manifest in peculiar final state signatures that can be distinguished
 494 from the soft interaction background.
 495 At high momentum transfer (perturbative regime), a proton can be described as a collection of par-
 496 tons, each bringing a fraction x of the initial beam momentum, whose distribution is described by
 497 the parton distribution functions (PDF), $f(x, Q^2)$, as a function of the Bjorken's variable and of the

3.2 CMS detector

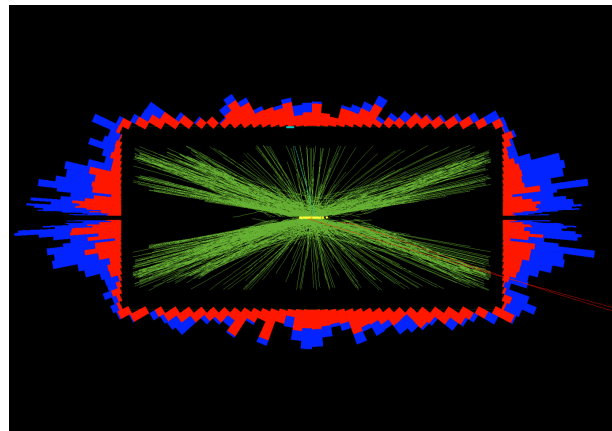


Figure 3.4: 78 events.

498 momentum transfer Q^2 . At very high center-of-mass energies (13 TeV), the proton masses can be
499 neglected; the available energy in the parton 1 and parton 2 scattering is unknown, $\sqrt{x_1 x_2 s}$. The
500 total cross-section is given by:

$$\sigma = \int dx_1 f_1(x_1, Q^2) \int dx_2 f_2(x_2, Q^2) \sigma_{12}(x_1 p_1, x_2 p_2, Q^2), \quad (3.4)$$

501 where σ_{12} is the cross-section at parton level, and f_1, f_2 are the parton PDFs. In fig. 3.5, parton
502 cross-sections are displayed as a function of the center-of-mass energy.

503 3.2 CMS detector

504 The Compact Muon Solenoid (CMS) is a multi-purpose detector built in the LHC ring. It is situated
505 in a cavern 100 m underground, near Cessy, in France. It is a cylinder 22 m long, with a diameter of
506 15 m, and a weight of 12500 tons. Its physics programme includes the search for the Higgs boson
507 (discovered in 2012), precision measurements of the Standard Model parameters and rare decays
508 (physics of beauty quark), and search for new physics beyond the standard model (SUSY, exotic
509 phenomena, dark matter, extra dimensions).

510 The CMS detector is structured in many layers of sub-detectors, giving different responses depend-
511 ing on the nature and the momentum of the particle passing through. The inner detectors have
512 been finely segmented in order to afford the high radiation levels and particle multiplicity at the
513 interaction point, so that the reduced occupancy of each layer allows to measure and distinguish
514 precisely the primary vertices of the hard interactions from the pile-up events. A very precise time
515 resolution is vital in order to synchronize all the subsystems together.

516 Fig. 3.6 shows a sketch of the CMS detector. It is longitudinally segmented in the barrel region and
517 two endcaps. In the forward region (over the endcaps), where the beam radiation is very intense,
518 additional calorimeters have been placed. In fig. 3.7, the mean path of a specific particle through
519 the sub-detectors is represented, depending on its flavour.
520

521 3.2.1 The coordinate system

522 The CMS coordinate system is depicted in fig. 3.8. x and y are the coordinates in the transverse
523 plane, z is the longitudinal coordinate. The x axis points at the center of the LHC ring, the y axis

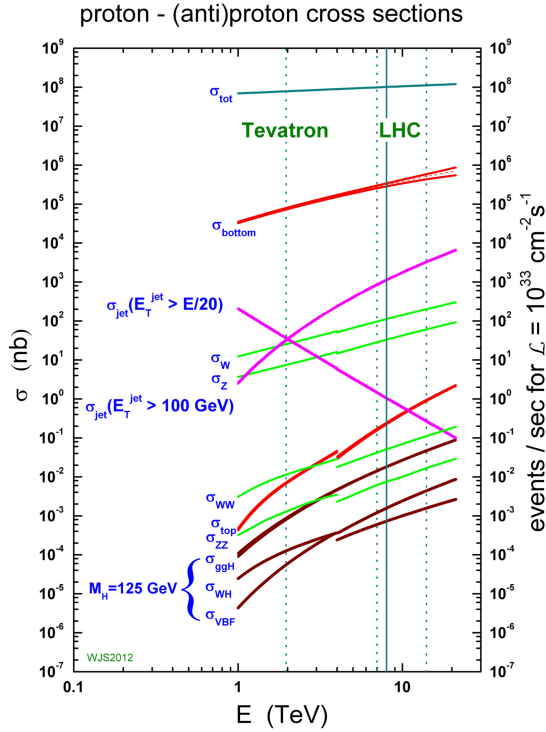


Figure 3.5: Cross-sections and number of expected events in proton-proton collisions, as a function of the center-of-mass energy. Rare phenomena, such as the Higgs boson production, can be observed at the LHC.

points upward, the z axis is along the beam direction. The azimuthal angle ϕ lies in the transverse plane, and it is measured starting from the x axis; the radial coordinate is r . The polar angle θ lies in the plane rz . The transverse component of the 3-momentum, \vec{p}_T , is orthogonal to the beam axis and lies in the plane xy . The transverse energy is defined as the magnitude of \vec{p}_T : $E_T = E \sin \theta$.

Two other commonly used variables are the rapidity, y , and pseudorapidity, η , defined as functions of the particle energy E , the longitudinal component of the momentum p_z and the 3-momentum modulus:

$$y = \frac{1}{2} \log \frac{E + p_z}{E - p_z} \quad (3.5)$$

$$\eta = \frac{1}{2} \log \frac{|\vec{p}| + p_z}{|\vec{p}| - p_z} = -\log \tan \frac{\theta}{2}$$

When the considered particle is produced in the forward region, hence at $\theta = 0$, $\eta \rightarrow \infty$. When the particle is produced in the transverse plane, hence $\theta = \pi/2$, $\eta = 0$. At high energies, when the masses can be neglected, rapidity and pseudorapidity coincide; these variables are largely used at colliders because they are invariant under Lorentz boosts along the beam direction.

3.2.2 The magnet

The CMS superconducting magnet is an hollow cylinder (13 m long, 6 m of diameter, showed in fig. 3.9). In the niobium and titanium fibers that constitute the solenoid, an electrical current of

CMS Detector

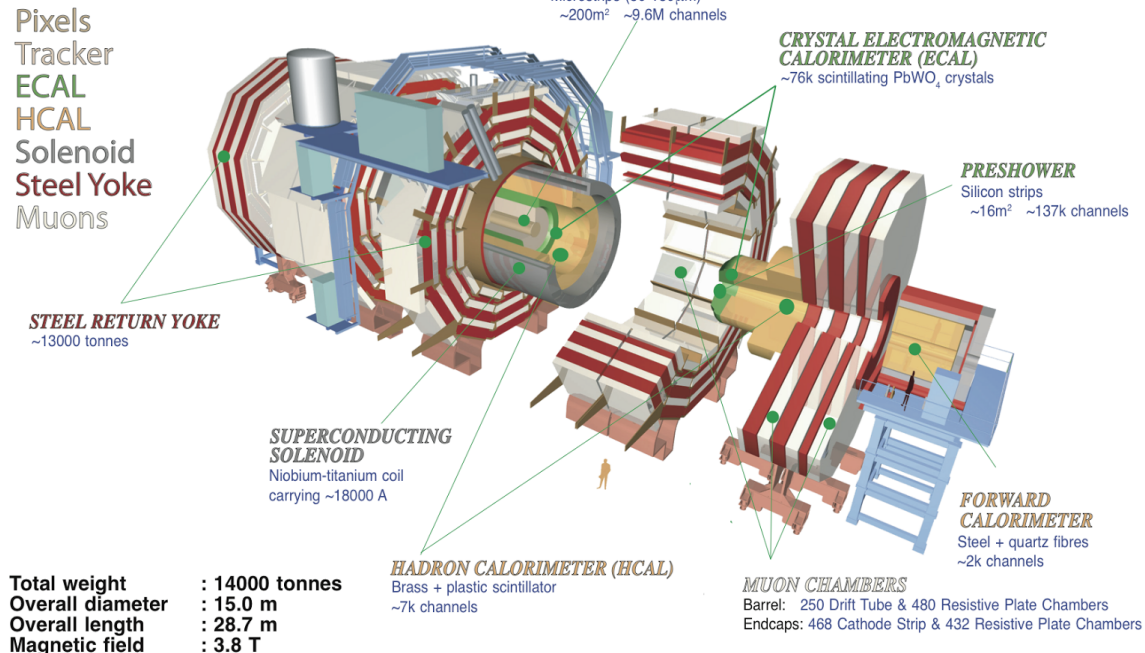


Figure 3.6: The CMS experiment.

539 19 kA flows, providing a maximum magnetic field of 3.8 T and storing a maximum energy of 2.6 GJ.
 540 Superconducting conditions are allowed by a liquid helium cooling system, keeping the solenoid at
 541 4.5 K. In order to avoid stray fields, the magnetic field lines are closed by the return yoke, composed
 542 by 10 ktons of magnetized iron blocks, located in the outer part of CMS and alternated to the muon
 543 chambers. The homogeneous magnetic field inside the detector bends the trajectories of the charged
 544 particles, allowing the measurement of their momenta p , given the relation with the magnetic field
 545 strength B and the radial coordinate R of the trajectory:

$$p[\text{GeV}] = 0.3 \times B[\text{T}] \times R[\text{m}]. \quad (3.6)$$

546 3.2.3 The tracking system

547 The CMS tracking system is composed by a cylinder of silicon detectors (2.5 m of diameter and 5.8
 548 m length). Their design allows a precise reconstruction of the tracks left by charged particles and of
 549 the interaction vertices, a fundamental tool to identify heavy quarks (charm, beauty) and leptons
 550 (taus). Tracker detectors cover a pseudorapidity region of $|\eta| < 2.5$ and have an active area of 210 m^2 .
 551 The two sub-detectors of the tracking system are the pixel detector, closer to the interaction point,
 552 and the strip detector, covering a radius of 0.2 – 1.2 m. The high granularity of the pixels and micro
 553 strips allows to keep the occupancy at acceptable levels, given the high multiplicity of the tracks (~ 1
 554 MHz/mm 2). The silicon detectors and the electronic cables are cooled down to a temperature of
 555 $\sim 10^\circ \text{C}$. The structure of the tracking system is showed in fig. 3.10.

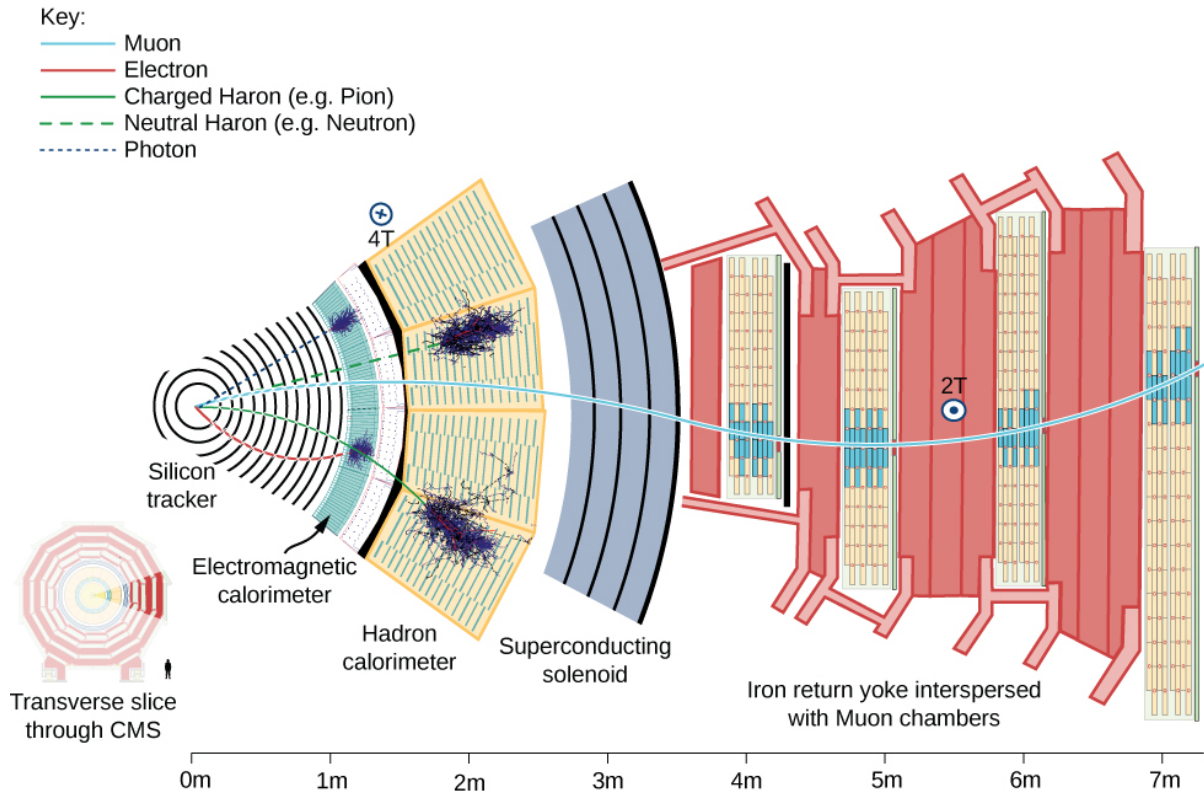


Figure 3.7: Mean path of a particle through the CMS detector. A muon, in light blue, passes through with a bended trajectory, depending on its momentum and charge, triggering signals in all the subsystems. An electron, in red, leaves a track in the silicon tracker and is absorbed by the electromagnetic calorimeter. A neutral or charged hadron, in green, stops inside the hadronic calorimeter. A photon, dotted blue line, showers in the electromagnetic calorimeter, without leaving any track in the silicon detector.

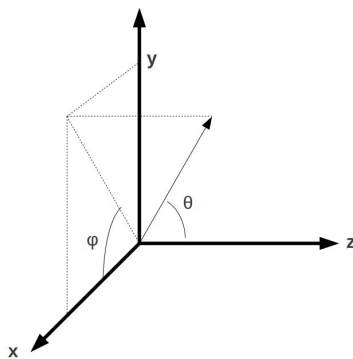


Figure 3.8: CMS coordinate system.

556 3.2.3.1 The pixel detector

557 The pixel detector is composed by 66 millions of silicon cells, whose dimensions are $100 \times 150 \mu m^2$,
 558 285 μm of thickness, placed in 1440 modules. Silicon cells are set in three layers in the barrel region
 559 and in two disks at each endcap. Barrel modules are disposed parallel to the magnetic field,
 560 whilst at the endcap they are tilted by about 20°. Pixels allow a spatial resolution of 10 μm in the

3.2 CMS detector

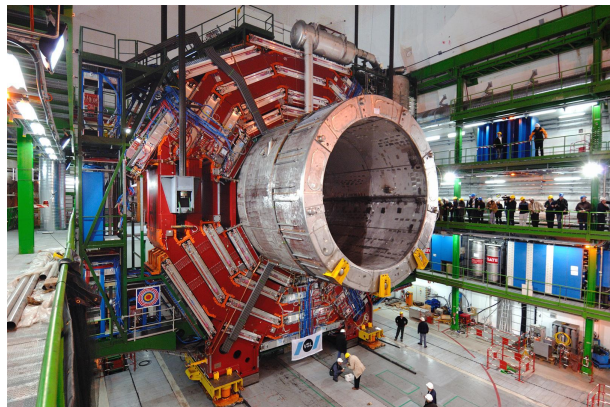


Figure 3.9: Installation of the superconducting solenoid in the CMS cavern.

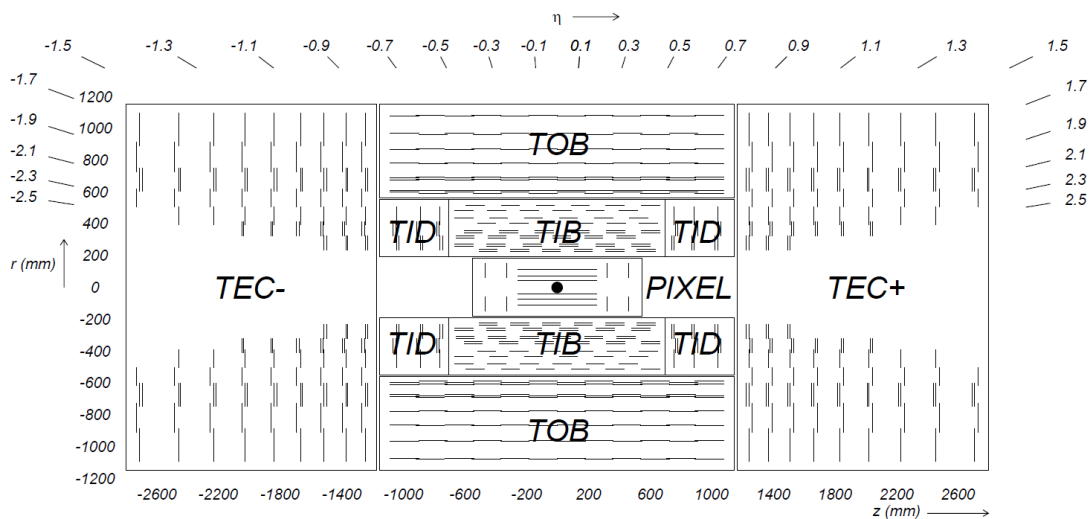


Figure 3.10: The CMS tracking system: the inner pixel detector, close to the interaction point, and the outer strip detector.

561 transverse plane, and of $\sim 20 \mu\text{m}$ along the longitudinal coordinate. Their reduced size guarantees
 562 an occupancy of 10^{-4} per pixel at each bunch crossing, in high luminosity regime.

563 **3.2.3.2 The strip detector**

564 The strip system is divided in the four-layered tracker inner barrel (TIB), covering a region $20 < r <$
 565 55 cm with respect to the interaction point, the six-layered tracker outer barrel (TOB), located at
 566 $55 < r < 110$ cm, the three tracker inner disks (TID) and the nine tracker endcaps (TEC) at each
 567 cylinder base. Given the lower radiation level at higher radii (and hence a lower occupancy, around
 568 few percent), micro strips are bigger than the pixels. Silicon strips in TIB and TID are $320 \mu\text{m}$ thick,
 569 10 cm long, and with a pitch ranging from 80 to $120 \mu\text{m}$; strips in TOB and TEC are 25 cm long, with
 570 a different thickness ($320 \mu\text{m}$ for TID, $500 \mu\text{m}$ for TEC) and pitch ($97\text{--}184 \mu\text{m}$). There are 15148 strip
 571 modules, and 9.3 million readout channels. The strip spatial resolution is about $20\text{--}50 \mu\text{m}$ in the
 572 transverse plane and about $200\text{--}500 \mu\text{m}$ along the longitudinal coordinate.

573 **3.2.4 The electromagnetic calorimeter**

574 The CMS electromagnetic calorimeter (ECAL, shown in fig. 3.11) is a homogeneous detector com-
 575 posed by lead tungstate (PbWO_4) scintillating crystals, designed to measure the energy deposits of
 576 photons and electrons through their electromagnetic showers. PbWO_4 is transparent and dense (8.3
 577 gr/cm³); it has a fast time response (the 85% of the scintillating light is emitted at every bunch cross-
 578 ing, namely 24 ns), high scintillating efficiency and radiation resistance; it has a radiation length is
 579 $X_0 = 0.89$ cm and a Molière radius of 2.19 cm. The ECAL is divided in the barrel region ($\eta < 1.479$,
 580 at a radius of 1.3 m) and the endcaps ($1.479 < \eta < 3$). The 61200 crystals employed in the barrel re-
 581 gion, whose size is (22×22) mm² \times 23 cm, have a radiation length of $25.8X_0$; the 7324 crystals in the
 582 endcaps, 28.6×28.6 mm² \times 22 cm, have a radiation length of $24.7X_0$. Before the endcaps, on each
 583 side, a pre-shower detector is installed: it is composed by two disks of lead absorber and two layers
 584 of silicon strips, up to a radiation length of $3X_0$. It has been designed to distinguish the photons
 585 coming from the π^0 decay from the rare Higgs decay $H \rightarrow \gamma\gamma$. The readout and amplification of the
 586 scintillating light, performed by avalanche photodiodes in the barrel and by vacuum phototriodes
 587 in the endcaps, requires a stable temperature of 18° C, mantained by a water cooling system.

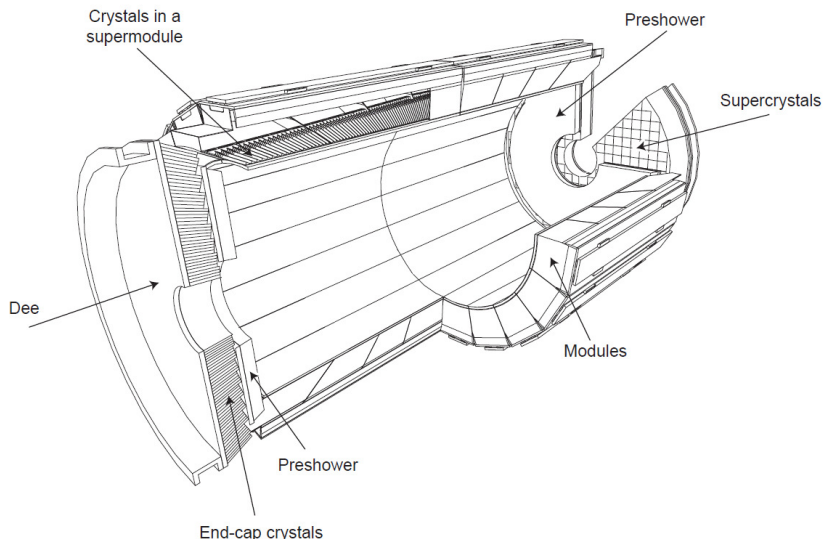


Figure 3.11: The CMS electromagnetic calorimeter.

588 **Controlla nuove calibrazioni** The energy resolution of the calorimeter is parametrized as:

$$\left(\frac{\sigma}{E}\right)^2 = \left(\frac{S}{\sqrt{E}}\right)^2 + \left(\frac{N}{E}\right)^2 + C^2, \quad (3.7)$$

589 where $S = 0.028 \text{ GeV}^{\frac{1}{2}}$ is the stochastic term, $N = 0.12 \text{ GeV}$ is related to noise contribution, and
 590 $C = 0.003$ is a constant term depending on the calibration.

591 **3.2.5 The hadronic calorimeter**

592 The hadronic calorimeter (HCAL, displayed in fig. 3.12) is a sampling calorimeter, composed by
 593 brass and plastic scintillator layers. It has been designed in order to guarantee a good hermeticity,
 594 allowing to perform a precise measurement of the missing transverse energy. It is located within
 595 the electromagnetic calorimeter and the solenoid, covering a region of $|\eta| < 1.3$ in the barrel, and

3.2 CMS detector

596 1.3 < | η | < 3 in the endcaps. Brass is non-magnetic and has short interaction length (16.4 cm):
597 the 60 mm thick absorber layers used in the barrel allow to reach 5.6 interaction lengths at $\eta = 0$
598 and 10.8 interaction lengths at $\eta = 1.3$; the 80 mm thick layers in the endcaps reach 11 interaction
599 lengths. An additional calorimetric layer has been installed out of the solenoid, in order to reach 11.8
600 interaction lengths in the barrel region. The scintillation light, typically in the blue-violet region of
601 the electromagnetic spectrum, is collected by wavelength-shifter fibers, translated and amplified
602 by multi-channel hybrid photodiodes, proportionally to the magnitude of the energy deposits. An
603 additional hadronic calorimeter has been placed in the forward region, 3 < | η | < 5.2, at 11.2 m from
604 the interaction point. It has been designed to afford the high levels of radiations: it is composed
605 by 55 mm thick absorber layers of stainless-steel, and quartz fibers, able to detect the Cherenkov
606 scintillating light of the charged particles of the hadronic showering. A longitudinally segmentation
607 allows to distinguish hadronic particles from electromagnetic components. The energy resolution
608 of the hadronic calorimeter is:

$$\left(\frac{\sigma}{E}\right) \approx \frac{a}{\sqrt{E}} + b\%, \quad (3.8)$$

609 where $a = 65\%$ in the barrel region, 85% in the endcaps, 100% in the forward region, and $b = 5\%$.

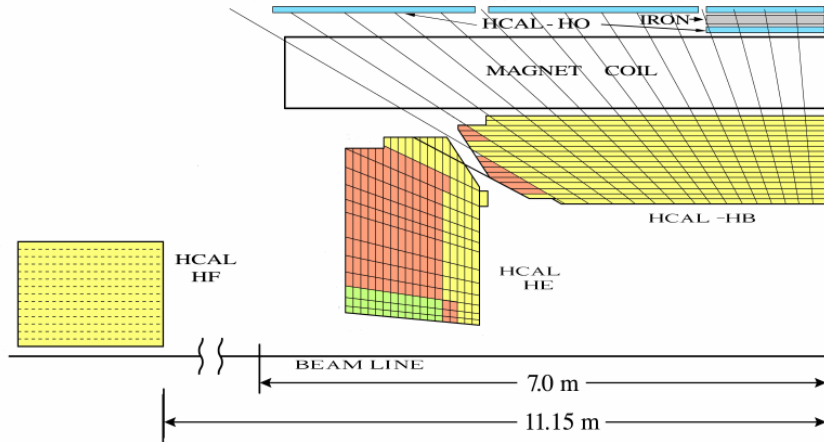


Figure 3.12: The CMS hadronic calorimeter.

610 3.2.6 The muon system

611 The outer system of the CMS experiment consists into gas detectors for identifying muons, that
612 are located between the iron return yokes, designed to close the magnetic field generated by the
613 solenoid. In the barrel region, where a smaller number of muons is expected and the magnetic field
614 is less strong, Drift Tubes (DT) detectors are installed. In the endcaps, where the flux of particles is
615 larger, Cathod Strip Chambers (CSC) are used, and disposed in three disks. CSCs are designed to
616 allow faster responses, higher granularity and radiation resistance. Resistive Plate Chambers (RPC)
617 are installed both in the barrel and in the endcaps as additional triggering system. The geometry of
618 the muon system is showed in fig. 3.13; it consists of 250 DTs, 530 CSCs, 610 RPCs, and it covers a
619 region | η | < 2.4.

620 3.2.6.1 The Drift Tubes

621 Drift Tube detectors cover a region of | η | < 1.2 and are arranged in four stations, segmented along
622 the beam line in five wheels. The basic element of the detector is the cell, that has a size $42 \times 13 \text{ mm}^2$.

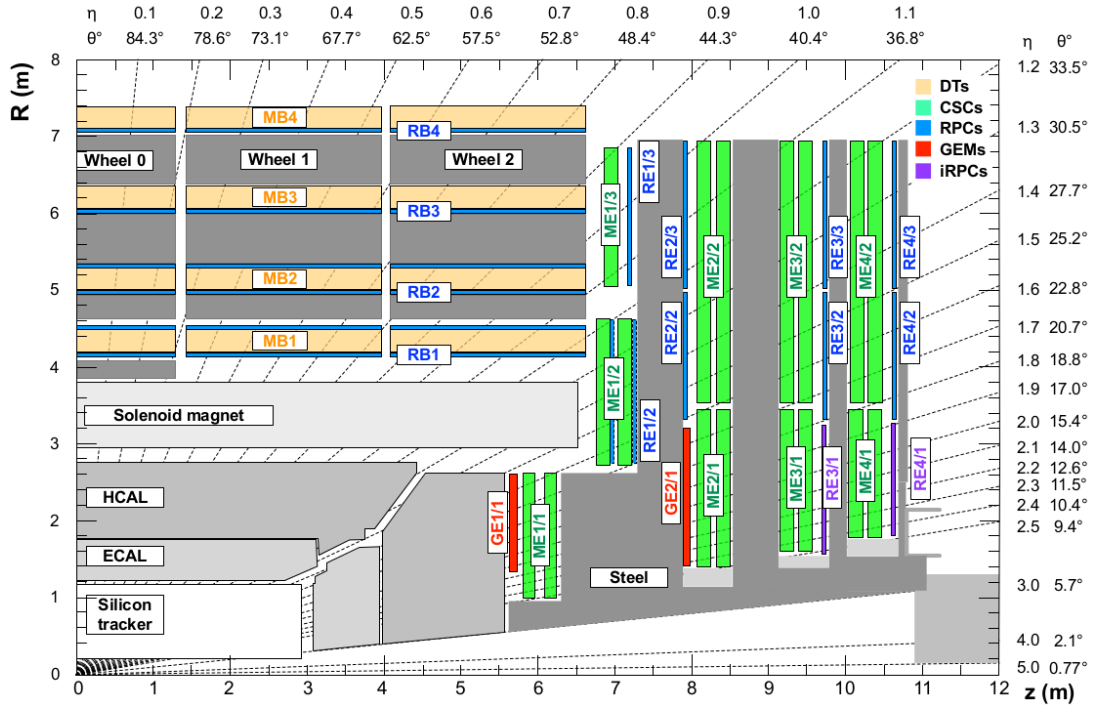


Figure 3.13: Section of CMS detector, in the plane $r\phi$, parallel to the beamline, that emphasizes the location of the muon detectors, in particular: Drift Tubes (DT, in yellow); Cathode Strip Chambers (CSC, in green); Resistive Plate Chambers (RPC, in blue).

623 Each cell is filled with a gas mixture (85% argon, 15% CO_2), in which the process of ionization takes
 624 places; the ionization electrons drift from the 50 μm thick steel anodic wire, in the center of the cell,
 625 towards the aluminium cathodic strips, located at its edge. Additional electrodes on the surface of
 626 the cells allows to shape the electric field, in order to make the drift speed of the electrons uniform:
 627 the muon position is then extrapolated from the measurement of the drift time. Every station is
 628 composed by three cells superlayers. In the inner and the outer superlayers, the cells are oriented
 629 such in a way that the anodic wire is located along the z axis, in order to measure the ϕ coordinate.
 630 In the intermediate superlayer, wires are parallel to the radial coordinate, hence they can measure
 631 the z position. The spatial resolution of the system is 100 μm in the $r\phi$ plane, 1 mrad in the ϕ
 632 coordinate, and 150 μm in the longitudinal z coordinate.

633 3.2.6.2 The Cathode Strip Chambers

634 Cathode Strip Chambers cover a region of $0.9 < |\eta| < 2.4$, overlapping with the DT in the pseudorapidity
 635 range $0.9 < |\eta| < 1.2$. The anodic wires inside each CSC are located into six planes, with the aim
 636 of measuring the radial coordinate; the wire planes are perpendicularly crossed by cathodic strips,
 637 disposed along the radial direction to measure the ϕ coordinate. Ionization electrons produced
 638 by muons passing through the gas mixture in the chambers migrate towards the anode, inducing
 639 a charge distribution on the cathodes, from which the azimuthal coordinate can be reconstructed.
 640 The spatial resolution in the r coordinate is 200 μm , and it is 75 – 150 μm in the $r\phi$ plane. CSCs are
 641 arranged in four disks and in three concentric rings.

3.2 CMS detector

642 3.2.6.3 The Resistive Plate Chambers

643 Resistive Plate Chambers (RPC) are located both in the barrel (disposed in six layers) and in the
644 endcap region (three layers), up to a pseudorapidity of $|\eta| < 1.6$. These gas detectors are charged
645 at very high voltages, in order to work in the avalanche ionization mode. The plastic resistive plates
646 are equipped with readout strips. The spatial resolution of the detector is low (1-2 cm), but the fast
647 timing response (2-3 ns) and good time resolution (1 ns) allow to employ RPCs as an additional
648 triggering system and to profit of a precise measurement of the bunch-crossing time.

649 3.2.7 The trigger system and data acquisition

650 The CMS trigger system has been designed considering the high instantaneous luminosity, such
651 that it can provide a fast response and it allows to reduce the nominal event rate of 40 MHz in proton
652 proton collision. The complexity of the CMS detector and the very high number of readout channels
653 result into a huge amount of data per event, approaching the order of few MB per bunch crossing,
654 hence 40 TB per second. The handling and the recording of data is currently limited at the order of
655 ~ 100 Hz; hence, applying online selections to skim the events that are going to be written on tape,
656 without rejecting interesting signals of hard processes and rare phenomena becomes a crucial and
657 challenging point for every data analysis. Events are filtered by trigger selections at different levels:
658 the Level-1 (L1) trigger is an hardware device, that allows to reduce the event rate from 40 MHz to
659 the order of 100 kHz; the High Level Trigger (HLT) is a set of software algorithms that skims the event
660 rate down to few hundred Hz. Once the trigger decisions are taken, the final events are handled by
661 the Data Acquisition System (DAQ), that collects the informations coming from to the subdetectors
662 and sends them to the storage devices.

663 3.2.7.1 The Level-1 trigger

664 The L1 trigger is an hardware device composed by customized electronics, and it accesses the in-
665 formations coming from the calorimeters and the muon system, while the tracker is not considered
666 given the excessively large bandwidth needed by its readout channels. The L1 trigger perform a
667 first raw local reconstruction of each object, called “trigger primitive”. The L1 trigger is composed
668 by three subsystems: the calorimeter trigger, the muon trigger (divided in three independent sub-
669 subsystems for each muon subdetector, namely DTs, RPCs and CSCs), and the global trigger, that
670 combines the informations of the former subsystems. The best quality trigger primitives recon-
671 structed by the calorimeter and muon detectors (namely, roughly reconstructed electrons, photons,
672 muons, jets, jets coming from the hadronic decays of tau leptons, and missing energy) are handled
673 by the global trigger, who takes the decision of discarding or keeping the event every $3.2 \mu\text{s}$. The
674 simplest trigger selections require the presence of a single object, whose energy or transverse mo-
675 mentum is higher than a certain threshold; more complicated triggers involve multiple objects or
676 geometrical selections, that can be performed in parallel up to 128 simultaneous requirements.

677 3.2.7.2 The High Level Trigger

678 The HLT skims the L1 output rate down to few hundreds of Hz by applying a set of algorithms imple-
679 mented in the same software used for the offline analysis, consisting in the event reconstructions
680 exploiting the whole informations coming from all subdetectors. The computing time is still a cru-
681 cial factor, hence selections applied to HLT physics objects are generally less accurate than those of
682 the offline analysis; furthermore, HLT can discard the event even before its full reconstruction (*i.e.*
683 by looking only at certain region of the detectors). Events filtered by the HLT decisions are assigned
684 to precise trigger paths and recorded in precise categories of datasets.

685 3.2.7.3 Data acquisition, computing and storage

686 The DAQ system deals with the storage, transfer and handling of the data collected by CMS; it also
687 supports and stores the data simulations and calibrations of the subdetectors. The CMS computa-
688 tional resources are located in worldwide distributed data nodes, called Tiers. The CMS software
689 (CMSSW) is based on an object oriented architecture (mainly C++). The basic unity of every data,
690 both real and simulated ones, is the Event, that could contain very rough informations (RAW data
691 format) or higher level refined objects (AOD, Analysis Object Data) where all the calibrations and
692 corrections needed to properly deal with the final physics objects are already in place. Data are
693 handled by C++ or python modules, and the outputs are written in ROOT files. [cittazione]

694 3.2.8 Particle Flow event reconstruction

695 The particle flow (PF) algorithm [ref. paper] aims at identifying and reconstructing each particle
696 produced by the proton-proton collisions, combining the informations coming from all the CMS
697 subdetectors. It is particularly suitable to improve the reconstruction of jets, missing transverse
698 momentum (used to identify neutrinos) and hadronically decaying tau leptons.
699 The association of the informations is performed at different stages. The reconstruction of the
700 charged particles in the silicon detector is performed with an iterative algorithm, and the recon-
701 structed object is called a tracker track. Then, a clustering algorithm is performed to collect and
702 combine the energy deposits in the calorimeters, in such a way to distinguish neutral from charged
703 particles, reconstruct their directions, improve the energy measurement of the very energetic charged
704 particles, whose tracks are less bended by the magnet and hence less precisely determined. The last
705 informations are provided by the hits collected in the muon system. The three sets of reconstruc-
706 tions are then combined with a link algorithm, that aims at associating tracker tracks to calorime-
707 ter clusters and muon hits with geometrical criteria. A track in the silicon detector is linked to a
708 calorimeter cluster if the extrapolated position lies in the cluster itself. Similarly, clusters in differ-
709 ent calorimeters are linked when the position in the more granular calorimeter (*i.e.* ECAL) lies in
710 the envelope of the clusters in the less granular calorimeter (*i.e.* HCAL). The decision of linking a
711 tracker track to a muon track is based on the χ^2 of a global fit between the two tracks.
712 The particle flow algorithm then interprets the collected and linked informations as different par-
713 ticles. Muons are identified by the combination of a track in the silicon detectors and a track in the
714 muon chambers. Photons are determined directly by ECAL clusters. Electrons energies and posi-
715 tions are measured by ECAL clusters, linked to a corresponding tracker track, and considering all
716 the energy clusters produced by the bremsstrahlung photons radiated while interacting with the
717 material. The hadrons are identified by the tracks (if charged) linked to the corresponding ECAL
718 and HCAL clusters. The hadron energy resolution, 10% at 100 GeV combining ECAL and HCAL, is
719 such that neutral hadrons can be distinguished as an energy calorimetric excess when overlapped
720 by a charged hadron occupying the same calorimetric towers. Finally, the missing transverse mo-
721 mentum is defined as the negative sum of the transverse momenta of all the particles identified by
722 the PF algorithm.

723

724 3.2.9 Physics objects**725 3.2.9.1 Track reconstruction**

726 The reconstruction of the trajectories of the charged particles passing through the CMS detector is
727 performed by multiple iterations of the Combined Track Finder algorithm, that is based on a Kalman
728 filter approach [73 A]; given the high multiplicity of particles produced at each bunch crossing and

3.2 CMS detector

729 the multiple scatterings throughout the detector materials, this represents a challenging task. The
730 CTF algorithm builds a track starting from the so-called seeds, namely triplets of hits collected in
731 the pixel detector inner layers, or couples of hits if the track originates from the interaction point.
732 The initial guess of the track given by the seeds is then extrapolated to the outer layers: if other hits
733 are found to be compatible with the trajectory hypothesis (χ^2 -based hypothesis test), they are added
734 to the track. Once the outer layers are reached, another reconstruction is performed backward, in
735 order to clean the track from spurious hits and enhance the tracking efficiency. The final collected
736 hits are re-fitted with Kalman Filter and more precise algorithms, in order to improve the quality
737 of the measurement. If two tracks share more than a half of their hits, the worst quality track is re-
738 jected. The track reconstruction efficiency for particles with $p_T > 0.9$ GeV is 94% in the barrel and
739 85% of the endcap region [72 A].

740

741 3.2.9.2 Electrons and photons reconstruction

742 Electrons are reconstructed combining a track with the energy deposits clustered in the ECAL, due
743 to the showering of the electron through the detector and the emission of bremsstrahlung photons.
744 The combination can proceed both from the silicon detector in the outgoing direction and in the
745 opposite way: the tracker seeding as starting point is suitable for low energy electrons, whose tra-
746 jectories are less bended and hence more accurately measured by the tracker system; the grouping
747 of ECAL clusters (called superclusters) followed by a consecutive track extrapolation, performed by
748 taking into account the electron interaction with the detector material, is more efficient in case of
749 high energetic electrons, due to the higher resolution of the ECAL scintillating crystals. A Gaussian-
750 sum filter algorithm (GSF) [ref 78 alberto] allows to properly take into account the effects of the
751 bremsstrahlung radiation, that is distributed not as a single Gaussian (standard Kalman filters) but
752 rather as a sum of Gaussian functions.
753 The identification of an electron relies on three groups of variables: observables combining mea-
754 surement performed in the silicon detectors and in the calorimeter; purely calorimetric observ-
755 ables; purely tracking informations. Different selections are used for electron candidates found in
756 the barrel and in the endcaps, and they can vary from loose criteria (high detection efficiency but
757 less purity, namely more contamination from object misidentified as electrons) to tight criteria.
758 Data and Monte Carlo simulations reproducing Z , ν and J/Ψ decays in e^+e^- are used to study the
759 optimal working points, each one targeting at a different purity.
760 The electron energy is determined correcting the raw energy measurement of the ECAL superclus-
761 ters by taking into account the effects of the losses due to radiation or gaps between the calorimeter
762 modules, and the pile-up contribution. The electron momentum resolution has been measured in
763 $Z \rightarrow e^+e^-$ decays in Run 1 LHC data, and it varies from 1.7 to 4.5% depending on the pseudorapid-
764 ity range. [arXiv 1502.02701]The electron isolation variable is defined as the p_T sum of the charged
765 and neutral particles laying in a cone of $\Delta R = 0.3$ around the electron trajectory, divided by the
766 transverse momentum of the electron:

$$I_{\Delta R=0.3}^e = \frac{\sum_{\text{char. hadrons}} p_T + \max[0, \sum_{\text{neut. hadrons}} p_T + \sum_{\text{photons}} p_T - 0.5 \sum_{\text{pile-up char. hadrons}} p_T]}{p_T^e}, \quad (3.9)$$

767 the contribution of the pile-up charged particles is removed. The isolation variable is used to dis-
768 tinguish electrons coming from the leptonic decays of electroweak bosons (low $I_{\Delta R=0.3}^e$) from elec-
769 trons coming from the decays of heavy fermions, when they are more likely produced in association
770 with light flavour jets and hence topologically close to calorimetric deposits due to hadrons (high

771 $I_{\Delta R=0.3}^e$).

772 Photons are reconstructed with the ECAL clusters only. Given their importance in the discovery of
 773 the Higgs boson, dedicated studies have been performed both in data and in Monte Carlo simula-
 774 tions reproducing the $H \rightarrow \gamma\gamma$ process. Particular care has been taken in the treatment of the photon
 775 conversions into electron-positron pairs while interacting with the tracker detector. Dedicated se-
 776 lections allow to define different photon identification working points. Similarly to the case of the
 777 electrons, the photon isolation variable can be defined. The photon energy resolution varies from
 778 1% to 3%, depending on the η range. [arXiv 1502.02702]

779 **3.2.9.3 Muon reconstruction**

780 A muon candidate can be built exploiting the hits collected in the silicon tracker (track) and in the
 781 muon system (standalone muon). Each muon subdetector (DTs, RPCs and CSCs) performs a local
 782 reconstruction of the candidate; the informations from the three muon chambers are combined
 783 with a Kalman filter approach.

784 Three different strategies are adopted to define a muon candidate in the CMS detector. A stan-
 785 dalone muon is reconstructed by only using the local reconstruction in the muon chambers. A
 786 tracker muon is built starting from a track in the silicon detector, that is extrapolated up to the muon
 787 chambers, taking into account the multiple scattering and the energy loss through the material.
 788 The tracker muon is defined if at least one segment, *i.e.* a short track built with CSCs or DTs hits,
 789 is matched to the starting track. This technique is the most efficient for the reconstruction of low
 790 energetic muons. A global muon is built starting from a standalone muon, and then its trajectory is
 791 extrapolated towards the inner layer of the silicon detector and eventually matched to a track; this
 792 approach is suitable for highly energetic muons ($p_T > 200$ GeV).

793 Different algorithms are used to assign the momentum to the muon candidate, in order to mitigate
 794 the effects of bremsstrahlung, that becomes significant when the muon approaches an energy of the
 795 order of 1 TeV. The radiated photons generate spurious hits in the chambers and larger occupancy,
 796 significantly deteriorating the momentum measurement.

797 Starting from 2016 Run, the muon reconstruction takes into account the Alignment Position Errors,
 798 namely the uncertainties due to the position of the muon chambers with respect to the silicon de-
 799 tectors. The final resolution on the muon momentum measurement depends on the p_T and η of the
 800 candidate, and ranges from 1% for very low momenta, up to $\sim 7\%$ ($|\eta| < 0.9$) – 10% ($1.2 < |\eta| < 2.4$).
 801 [DP2016_067]

802 The muon isolation $I_{\Delta R=0.4}^\mu$ is defined similarly to the electron isolation, but by taking into account
 803 a larger cone $\Delta R = 0.4$ around the muon direction.

804 **3.2.9.4 Jet reconstruction**

805 The nature of the strong interaction is such that coloured partons, namely quarks and gluons, are
 806 forced to aggregate to form a color-neutral hadron, in the process called hadronization. Therefore,
 807 partons cannot be observed as free particles in a detector, but rather as collimated jets of hadronic
 808 particles.

809 Jets are reconstructed starting by the PF candidates in the event. The charged hadron subtraction
 810 algorithm (CHS) removes candidates not associated to the primary vertex in order to remove con-
 811 tributions from pileup [39]. The remaining particles are used as input to jet clustering algorithms to
 812 reconstruct particle-flow jets. The jets are clustered using the FASTJET package [?] with the anti- k_T
 813 jet sequential clustering algorithm [40]. A sequential clustering algorithm is designed in order to be
 814 infrared and collinear safe, namely, if the final state particles undergo a soft emission or a collinear

3.2 CMS detector

815 gluon splitting, the number and shapes of the jets should not change. The starting point of a sequen-
816 tial clustering algorithm is the definition of the distances between two particles i and j , and the
817 distance of a given particle i from the beam-spot B :

$$d_{ij} = \min(p_{T,i}^{2a} p_{T,j}^{2a}) \frac{R_{ij}^2}{R^2}, \quad (3.10)$$
$$d_{iB} = p_{T,i}^{2a}$$

818 where $p_{T(i,j)}$ are the transverse momenta of the particles, $R_{ij}^2 = (y_i - y_j)^2 + (\phi_i - \phi_j)^2$ is the angular
819 distance between the particles, a is an exponent depending on the clustering algorithm chosen,
820 and R is the clustering parameter. The algorithm then operates as follows:

- 821 • it computes all the possible combination of distances d_{ij} and d_{iB} and it finds the minimum;
- 822 • if the minimum is d_{ij} , the four-momenta of the particles i and j are summed up in one can-
823 didate $i\bar{j}$; i and j are removed from the list of candidates, the distances are updated, and the
824 algorithm proceeds to re-calculate all the possible remaining d_{ij} ;
- 825 • the clustering stops when the smallest quantity is d_{iB} : i particle is defined as one jet, and it
826 is removed from the list of particles;
- 827 • this process is repeated until all the particles are assigned to a jet, that must be separated from
828 another jet at least by a distance $R_{ij} > R$.

829 In case of the anti- k_T algorithm, $a = -1$. It tends to cluster high p_T particles first, since the hard
830 term dominates d_{ij} in equation 3.10. Since the soft particles have lower impacts, the shape of the
831 jet is not sensitive to the soft radiation and rather stable against the softer pile-up contributions.

832 In this analysis, clustering parameters of $R = 0.8$ and $R = 0.4$ will be used to define the “fat”-jets or
833 AK8 jets, and the “standard”-jets or AK4 jets). In order to avoid double-counting of PF candidates,
834 AK4 jets are considered only if the angular separation from the leading AK8 jet is larger than $\Delta R >$
835 0.8.

836 Since the detector response to different particles is not linear, particular care should be taken in the
837 assignement of the measured momentum of the clustered jet to the corresponding true value of the
838 original parton [41]. A set of jet energy corrections (JECs) are applied sequentially and with a fixed
839 order. Each correction constists in a rescaling of the jet four-momentum, and it takes into account
840 different effects that are factorizes.

- 841 • The L1 JECs remove the effect of the pile-up; they consist into an offset correction of the jet
842 p_T . They are determined from Monte Carlo (MC) simulations of dijet events produced by
843 strong interaction with and without pile-up events on top, and parametrized as a function of
844 kinematical parameters (jet area, pseudorapidity and p_T) and of the average p_T density per
845 unit area ρ . Residual difference between data and the detector simulation are evaluated in
846 data collected with a random trigger, called zero bias, applying the only requirement of the
847 beam crossing happening. Pile-up offset corrections are displayed in fig. 3.14 (top left), as a
848 function of the jet pseudorapidity.
- 849 • The simulated response of the detector is not uniform over jet p_T and η . This effect is miti-
850 gated by the L2L3 MC-truth corrections. They are calculated in MC simulations of dijet events
851 by taking into account the discrepancy between the reconstructed p_T of the jet and the true
852 p_T at particle level, as a function of jet p_T and η . L2L3 scale factors describing the simulated
853 jet response are reported in fig. 3.14 (top right), as a function of the jet pseudorapidity.

- 854 • The small data-MC discrepancies ($\sim 1\%$) left after applying the previous set of JECs are cor-
 855 rected by the L2 and L3 residual corrections. The L2Residuals are calculated in dijet events,
 856 as a function of p_T . The L3Residuals are calculated in $Z \rightarrow (\mu\mu, ee) + \text{jet}$ events, photon +
 857 jet events and multijet events, as a function of η and p_T , with the p_T -balancing method [41].
 858 Data-MC scale factors for L2L3Residuals are displayed in fig. 3.14 (bottom), as a function of
 859 the jet η and p_T .
- 860 • An optional correction, not used in this analysis, is the L5 flavor-dependent correction, that
 861 is extracted from MC simulations.

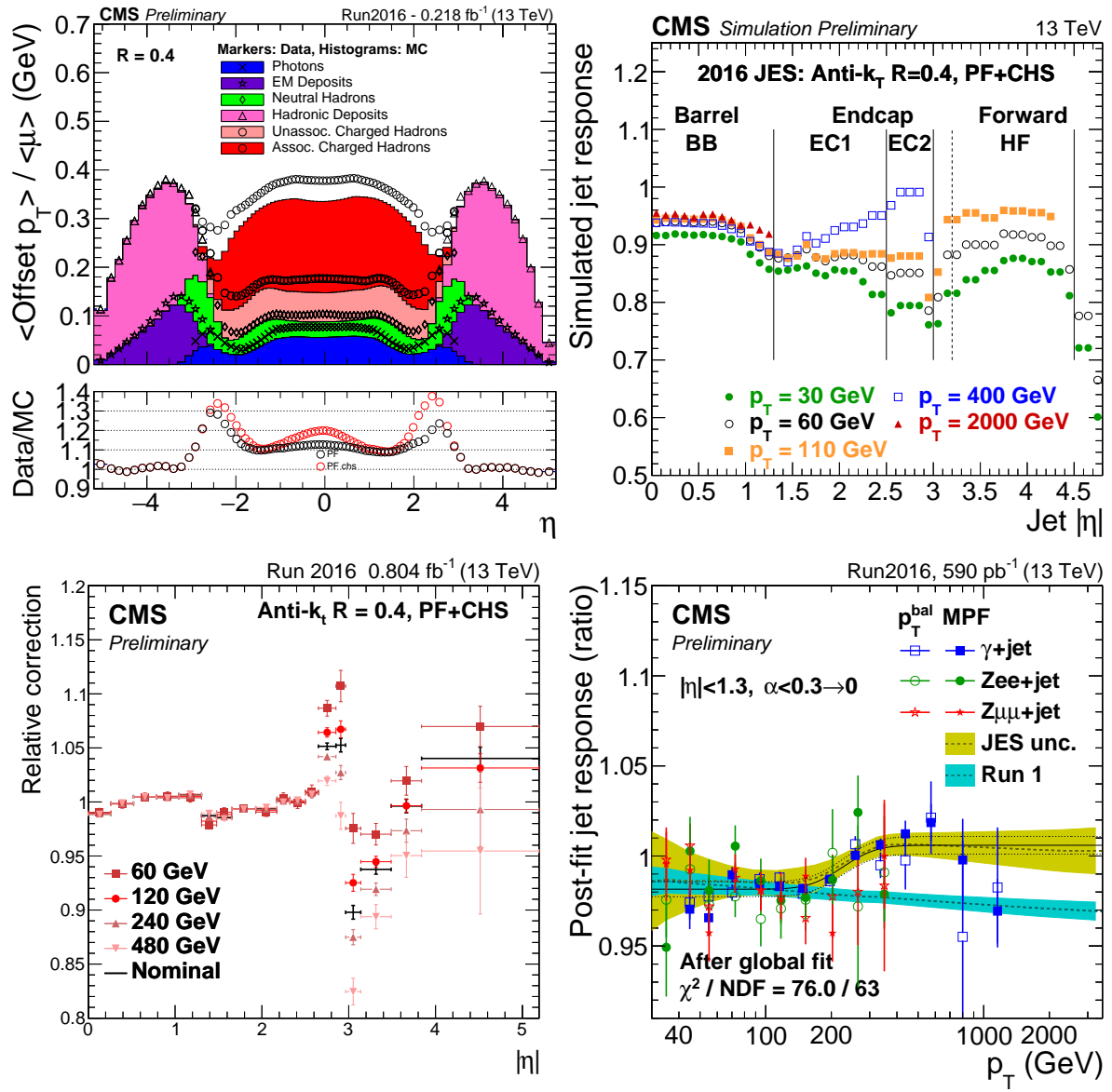


Figure 3.14: Top left: average p_T offset due to additional pile-up events, measured both in data and in MC simulations, as a function of the jet pseudorapidity. Top right: simulated jet response (L2L3 MC-truth corrections), as a function of the jet pseudorapidity. Bottom left: L2L3 residual data-MC corrections, evaluated on dijet events, as a function of the jet η . Bottom right: L2L3 residual data-MC corrections, evaluated on dijet and $Z/\gamma + \text{jet}$ events, as a function of the jet p_T .

3.2 CMS detector

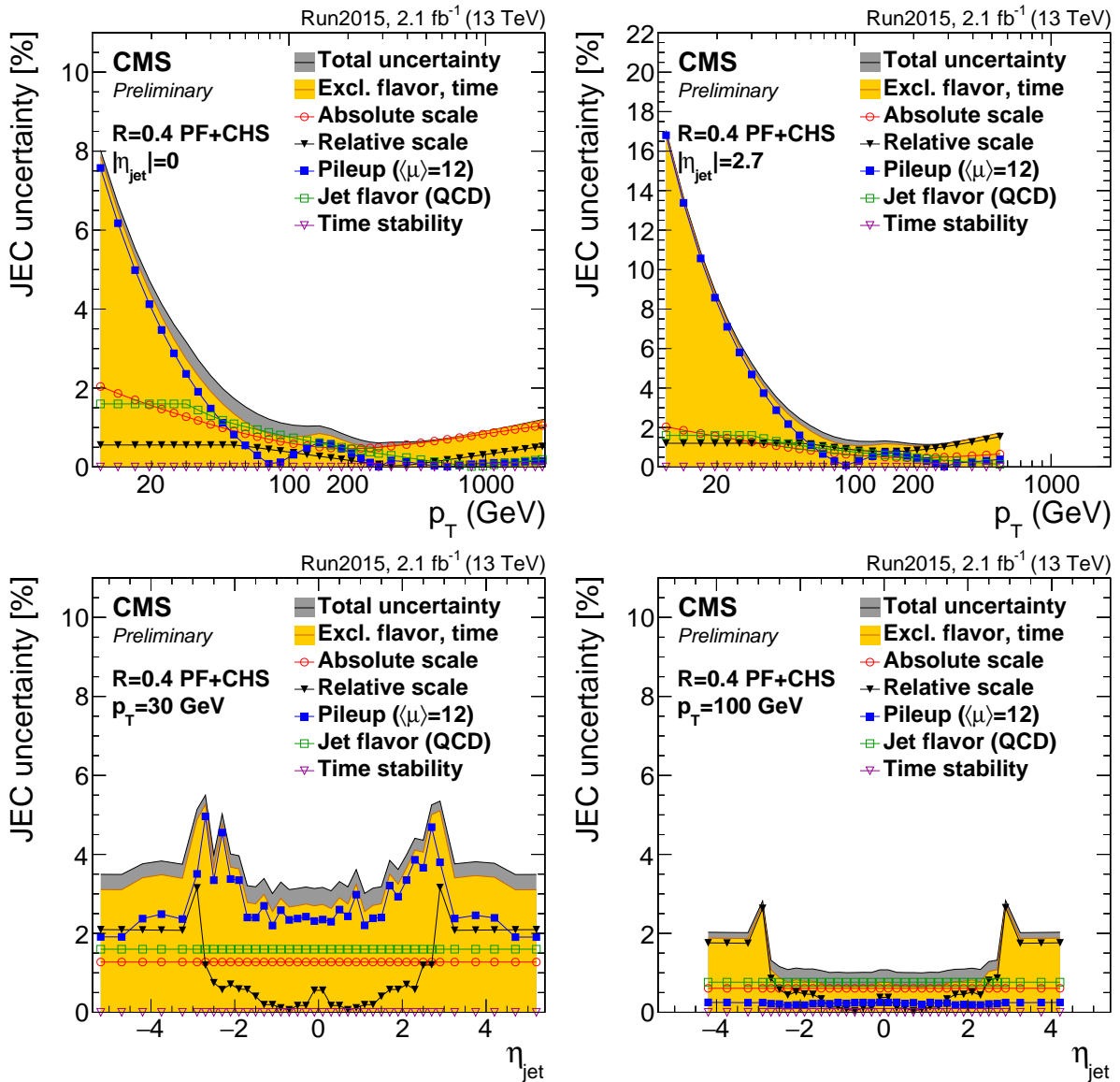


Figure 3.15: Jet energy corrections uncertainties, as a function of jet p_T (top) and η (bottom), calculated in 2015 data. The yellow histograms report the convolution of the uncertainties applied in the analysis.

862 Each jet energy correction is determined with an uncertainty, and reported in fig. 3.15 for 2015 data,
 863 as a function of p_T and η of the jet. The total uncertainty for jets with p_T larger than 30 GeV (100
 864 GeV) is smaller than 3% (1%) in the barrel, and up to 5% (3%) in the endcaps.

865 An additional effect that must be taken in account is the discrepancy in the jet energy resolution
 866 (JER) observed in data and in Monte Carlo samples. A smearing procedure is applied in MC simula-
 867 tions (described in detail in sec. 4.2.6), in order to restore a better agreement. Jet energy resolutions
 868 in Monte Carlo simulations are displayed in fig. 3.16 (top), as a function of the jet p_T and the average
 869 number μ of reconstructed primary vertices, considering central (left) and forward (right) jets. The
 870 resolution is stable against the pile-up for jet $p_T > 100$ GeV, and it ranges from 10% at 100 GeV, down
 871 to 4% at 1 TeV. In fig. 3.16 (top). In fig. 3.16 (bottom), data-MC smearing scale factors are reported
 872 as a function of η .

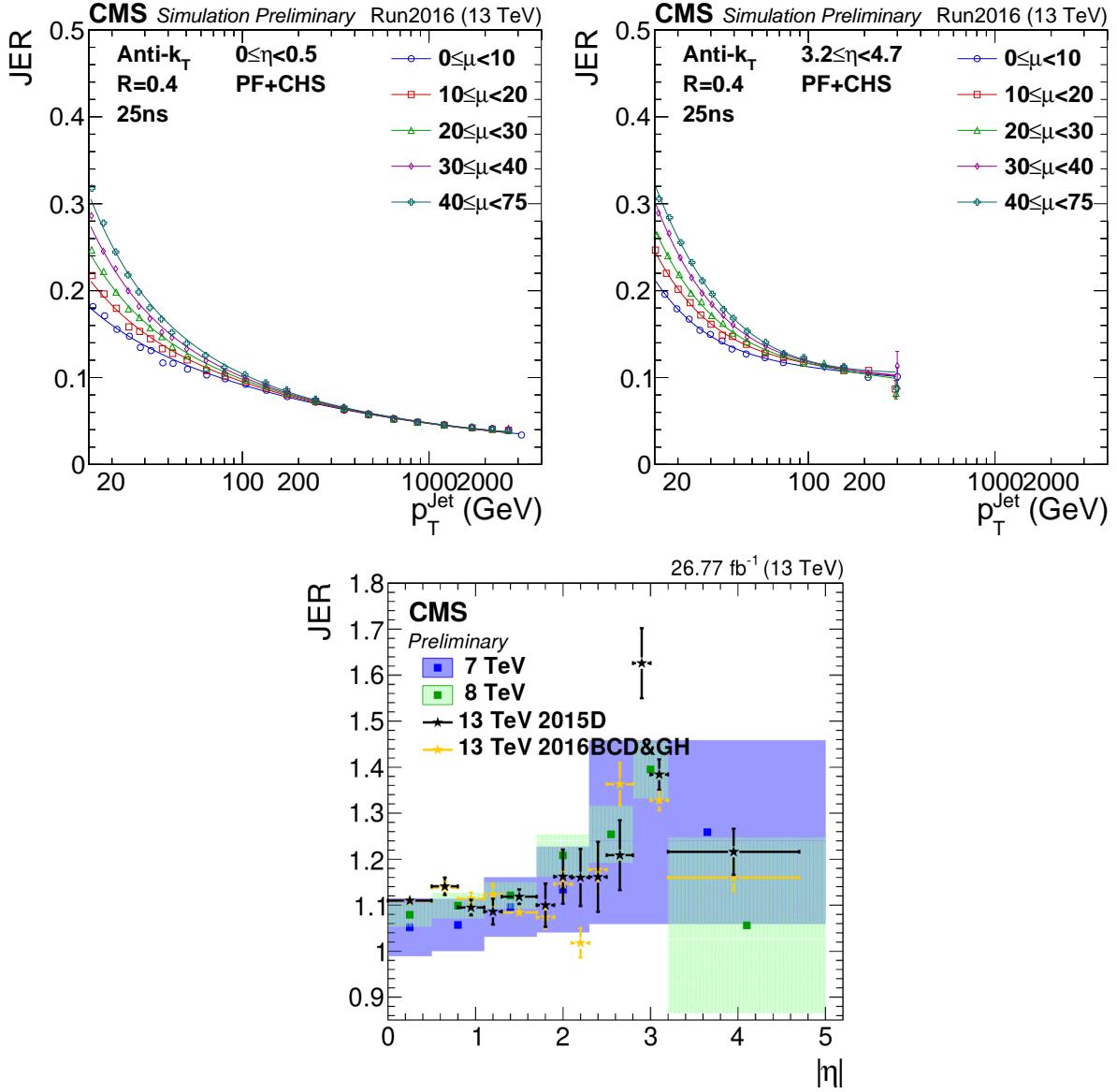


Figure 3.16: Top: jet energy resolution in MC simulations, as a function of the jet p_T . Different curves represent a different average number of primary vertices per event (μ). Bottom: data-MC scale factors, as a function of the jet η , measured in 2016 data (yellow dots).

3.2.9.5 Tau reconstruction

Tau leptons have a very small lifetime ($\sim 3 \times 10^{-13}$ s), hence they decay before reaching the pixel detector and they can only be reconstructed through their decay products. Approximatively 60% of the times, τ leptons decay in hadrons, hence they are reconstructed as small collimated jets in the CMS detector. The main decay modes of the hadronic tau, τ_h , are one or three charged mesons (mainly π^\pm), also in association with a π^0 decaying in a couple of photons, and a τ neutrino. Hence, photons and charged hadrons are the main ingredients of dedicated algorithms to perform the τ_h reconstruction and identification, in order to distinguish them from quark and gluon-initiated jets. The main CMS τ_h reconstruction algorithm, Hadron Plus Strips (HPS) [42], is particle-flow based. HPS builds the tau candidate from a PF jet, clustered with the anti- k_T algorithm with $R = 0.5$, and it

3.2 CMS detector

883 reconstructs the $\pi^0 \rightarrow \gamma\gamma$ decays within the jet cone, by taking into account the photon conversions
884 in the silicon detector. The exploitation of the PF informations is such that the HPS algorithm shows
885 stable performances in the reconstruction of the τ_h energy as a function of the energy itself. The
886 τ_h candidate is required to be isolated, namely no energy deposits other than the τ decay products
887 should be present in the tau cone. Depending on the low threshold set to consider the surrounding
888 particles as included in the cone, different isolation working points can be defined. With the looser
889 working point, the probability of misidentifying a quark or gluon jet as a tau is around 1% [42].

890 **3.2.9.6 b-jets tagging**

891 The bottom quark plays a fundamental role in numerous standard model processes, *i.e.* the physics
892 related to the top quark (whose decay into a W and a b-quark with a branching fraction of 100%) and
893 the Higgs boson (decaying into $b\bar{b}$ with a branching fraction $\sim 60\%$). Many algorithms have been
894 exploited by the CMS collaboration, with the aim of distinguishing a b-quark initiated jet and jets
895 originating from light quarks or gluons [43]. The most remarkable feature of the b-quark is the long
896 lifetime (~ 1.5 ps), that has the experimental consequence of a displaced decays (few mm) with re-
897 spect to the primary vertex. The direct leptonic decays of the b-quark (into μ and e) or the cascade
898 leptonic decays involving c-quarks give an additional handle to its identification.
899 Given the high spatial resolution of the silicon detector, track reconstruction is a key point of the
900 b-tagging procedure. Tracks inside a jet candidate must satisfy criteria related not only to their
901 quality but also on their distance from the interaction point. The track impact parameter is the dis-
902 tance between the primary vertex and the coordinate of closest approach. Tracks that are too far
903 from the interaction point are discarded, in order to suppress the pile-up contributions. The Com-
904 bine Secondary Vertex (CSV) algorithm [44] sorts jet candidates in categories, based on the number
905 of reconstructed secondary vertices (one reconstructed secondary vertex, no vertex but two tracks
906 with high impact parameters, and the remaining cases). A multivariate approach allows to train the
907 algorithm over the categories, considering as discriminating variables both tracking informations
908 (numbers and properties of the tracks) and their relations with the secondary vertex reconstruction
909 (impact parameters; angular, linear, 2D and 3D distances of the vertex from the tracks and the jet
910 axis, and the invariant mass of the charged particles associated to the secondary vertex).
911 By tuning the different selections, working points with different efficiencies have been set. The loose
912 working point, used in this analysis, has a 90% signal efficiency and a 40% misidentification rate.
913 The b-tagging efficiency is different in data and in simulations. Multiplicative scale factors are cal-
914 culated in events enriched in b-quark jets.
915

916 **3.2.9.7 Missing transverse energy reconstruction**

917 Neutrinos can interact with the other particles only via the electroweak interactions; hence, when a
918 neutrino is produced in the proton-proton collisions, it passes through the CMS experiment, unde-
919 tected. Its only experimental signature is the momentum imbalance (\vec{p}_T^{miss}) in the transverse plane
920 $r\phi$. The magnitude of \vec{p}_T^{miss} vector is also called missing transverse energy, E_T^{miss} . Given its defi-
921 nition, it is evident that E_T^{miss} is a delicate variable to deal with, since it depends on all the other
922 objects, on their imperfect measurements, on the detector noise and the pile-up events.
923 The PF E_T^{miss} is the negative sum of the transverse momenta of the PF candidates reconstructed in
924 the event. Inefficiencies in the tracker reconstruction and non-linear responses of the calorimeters
925 can be corrected by propagating the jet energy corrections to \vec{p}_T^{miss} :

$$\vec{p}_T^{\text{miss,corr}} = \vec{p}_T^{\text{miss}} - \sum_{j \in \text{jets}} (\vec{p}_{T,j}^{\text{corr}} - \vec{p}_{T,j}^{\text{raw}}), \quad (3.11)$$

926 where "corr" ("raw") is related to corrected (raw) p_T of the considered jet. This correction is known
 927 as the "Type-I" correction to E_T^{miss} . Jets included in the calculation are AK4 with CHS algorithm
 928 applied to remove the pile-up contribution, they must have $p_T > 15 \text{ GeV}$ and less than 90% of their
 929 energy deposited in the electromagnetic calorimeter. If a muon lies in the jet cone, it is subtracted
 930 from the jet and added after the p_T correction. A similar correction is performed to correct \vec{p}_T^{miss} at
 931 trigger level; in this case, a jet p_T threshold of 35 GeV is chosen.
 932 The topology of the final state affects the E_T^{miss} uncertainties; hence, they are factorized considering
 933 the effects

934 To estimate the uncertainty on the E_T^{miss} , one can factorize it into its components of jets, elec-
 935 trons, muons, taus, photons and jets of $p_T < 10 \text{ GeV}$ and PF candidates not within jets (defined as the
 936 unclustered energy) and vary each object within its scale and resolution uncertainties. For the un-
 937 clustered energy uncertainty the low energy PF particles are further divided into groups to account
 938 for the res- olution effect of different detector components: charged PF hadrons (dominated by the
 939 tracker resolution), neutral PF hadrons (dominated by the HCAL resolution), photon PF candidates
 940 (dominated by the ECAL resolution) and PF candidates associated with the forward hadronic (HF)
 941 calorimeter (dominated by the forward HCAL resolution). The largest contributions to the unclus-
 942 tered energy uncertainty are due to the neutral PF hadrons and HF PF candidates. The magnitude
 943 of the uncertainties due to jet energy scale correction and unclustered energy scale variations are
 944 found to be 5% and 30% respectively in an inclusive ttbar simulation.

945 3.3 ATLAS, ALICE, LHCb detectors

946 3.3.1 ATLAS

947 ATLAS (A Toroidal LHC ApparatuS) is a multi-purpose experiment, that shares the same scientifical
 948 aims of CMS. The simultaneous observation of an Higgs boson-like particle at the two experimental
 949 facilities represented an irrefutable proof of the discovery of the Higgs boson.
 950 ATLAS has a cylindrical shape (diameter of 25 m, length of 46 m) and weights 7000 tons. Like CMS,
 951 ATLAS is composed by many sub-detectors: trackers, calorimeters and muon system. The ATLAS
 952 magnetic field is provided by a solenoid, located inside the cylinder, and a big toroid, located outside
 953 the sub-detectors, able to reach a magnetic field of 2 T at the interaction point. The main differences
 954 among the two experiments are listed below.

- 955 • *Tracker* – the CMS tracker has a better p_T resolution (mainly due to the higher magnetic field):
 956 $\sigma_{p_T}/p_T \approx 5 \cdot 10^{-4} p_T + 0.01$ at ATLAS; $\sigma_{p_T}/p_T \approx 1.5 \cdot 10^{-4} p_T + 0.005$ at CMS.
- 957 • *Electromagnetic calorimeter* – the CMS electromagnetic calorimeter is completely enclosed
 958 inside the solenoid, whilst ATLAS calorimeter is outside of the solenoid. The particles going
 959 through the solenoid suffer an energy loss and a consequent deterioration of the energy res-
 960 olution. The CMS ECAL has an enery resolution of $\sigma_E/E \approx 3\%/\sqrt{E}$; the ATLAS calorimeter
 961 has a sandwich structure (liquid argon and lead layers) and a resolution of $\sigma_E/E \approx 10\%/\sqrt{E}$.
- 962 • *Hadronic calorimeter* – the CMS HCAL is partly inside the solenoid, partly outside, depauper-
 963 ating the resolution. The ATLAS hadronic calorimeter (made of iron and plastic scintillator
 964 tiles) has an energy resolution $\sigma_E/E \approx 50\%/\sqrt{E} + 0.03 \text{ GeV}$; CMS HCAL has a resolution of
 965 $\sigma_E/E \approx 100\%/\sqrt{E} + 0.05 \text{ GeV}$.
- 966 • *Muon system* – the peculiar geometry of the ATLAS muon system allows a better resolution of
 967 the standalone measurement of the muon momenta (*i.e.*, without using tracker and calorime-
 968 ters), that is around 10% at 1 TeV. CMS has better performance when combining the informa-

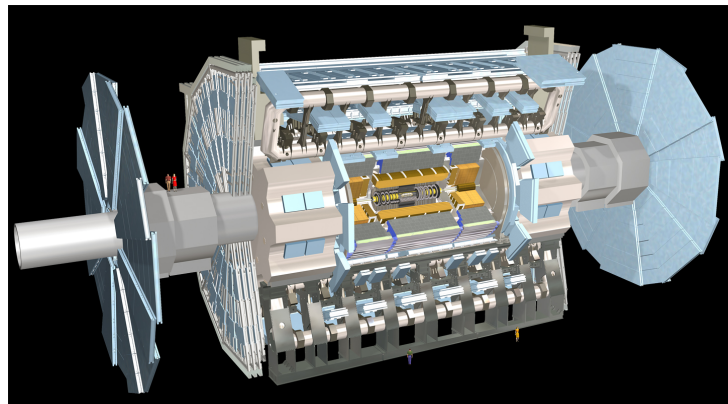


Figure 3.17: The ATLAS experiment.

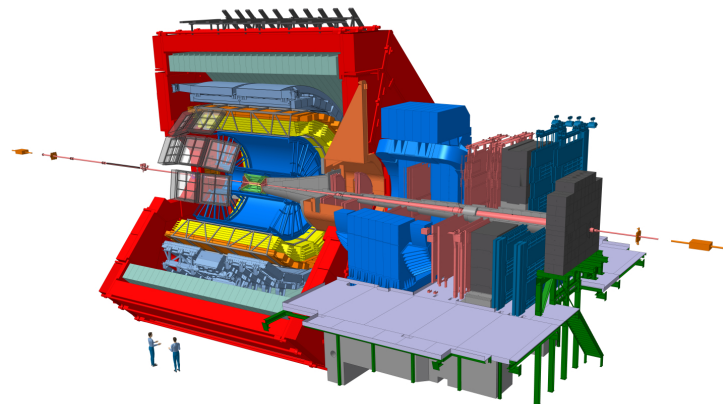


Figure 3.18: The ALICE experiment.

969 tions coming from the inner detectors (7% at 1 TeV against the 35% for the standalone mea-
970 surement).

971 **3.3.2 ALICE**

972 ALICE (A Large Ion Collider Experiment) studies the heavy ion collisions (lead-lead) or proton-ion
973 in order to explore the physics of the hadrons in high density (or temperature) regimes, when a new
974 state of matter appears, the so-called quark-gluon plasma (QGP). The QGP played a crucial role in
975 the very first instants of life of the universe.

976 **3.3.3 LHCb**

977 LHCb (Large Hadron Collider beauty) is a detector designed to study the b quark properties, in par-
978 ticular the CP violation and other rare phenomena involved in b hadrons. The final aim of these
979 measurements is trying to solve the matter-antimatter asymmetry problem.

980 The three detectors are depicted in fig. 3.17–3.19.

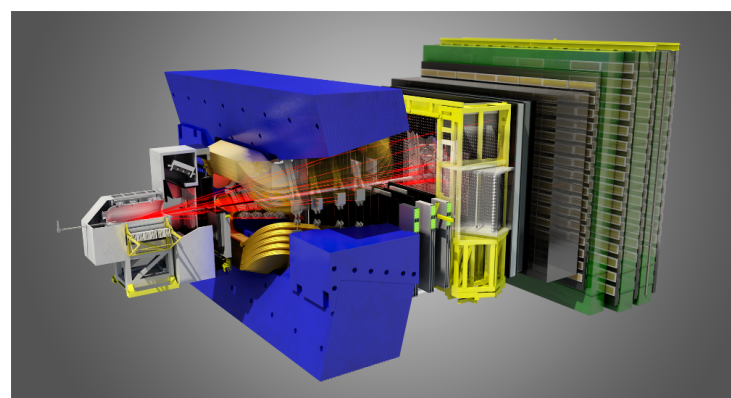


Figure 3.19: The LHCb experiment.

981

Chapter

4

Search for diboson resonances in the $ZV \rightarrow \nu\bar{\nu}q\bar{q}$ final state

982

983

984 Brief intro to the analysis

985 **4.1 Data and Monte Carlo samples**

4.2 Event selection

4.2 Event selection

In this section, a list of the physics objects used in the analysis is presented, together with performance and validation plots.

The objects are selected according to the standard Run2 recommendations provided by the various POGs for the Summer16 (25ns) MiniAOD-v2 (Moriond recommendations).

The version of CMSSW used for the analysis is CMSSW_8_0_25.

4.2.1 Vertex and Pile-up

How the vertices and pile-up are reconstructed

Due to pileup several primary vertices are typically reconstructed in an event. The primary vertex of the event is defined as the one with the highest sum of transverse momenta $\sum p_T^2$ of clustered physics objects associated to it, which passes the following selections:

- number of degrees of freedom $N_{DoF} > 4$
- vertex position along the beampipe $|z_{vtx}| < 24\text{cm}$
- vertex distance with respect the beam pipe $d_0 < 2\text{cm}$

where z_{vtx} and d_0 are the distance along and perpendicular to the beam line of the vertex with respect the nominal interaction point $(0, 0, 0)$.

The data sample contains a significant number of additional interactions per bunch crossing, an effect known as pileup (PU).

The Summer16 v2 MINIAOD Monte Carlo samples are generated simulating the PU conditions, using the 25ns asymptotic PU scenario. Nevertheless, the MC PU description does not match exactly the conditions in data, and there is therefore the need to reweight the simulated events in order to improve the agreement with the data.

The MC samples are reweighted using the standard CMS PU reweighting technique [45, 46] assuming a total inelastic cross section of $\sigma_{in} = 69\,200\mu b$.

The comparison between the distributions of primary vertices in data and MC after the PU reweighting is applied is shown in Figure 4.1 for an event selection (called inclusive selection) requiring large amount of \vec{p}_T^{miss} recoiling against an AK8 fat jet (Tab. ??).

Figure 4.1: Primary vertices distributions after reweighting with the official recipe and $\sigma_{in} = 69\,200\mu b$.

4.2.2 Electrons

How the electrons are reconstructed: The electron identification variables that have been found to be the most powerful, and are used in the selection, are: the energy-momentum match between the seed cluster and the trackE seed/pin, the variables measuring spatial matching between the track and the supercluster, in and in, the supercluster width, i i(as taken from the covariance matrix using logarithmic weights), and the hadronic leakage variable H/E. The supercluster width is to a very good approximation unaffected by the spreading due to the magnetic field of the showering in the tracker material.

Isolation variables are computed in three sub-detectors: the tracker, the ECAL, and the HCAL. Transverse energy/momentun sums are evaluated in regions of $R < 0.3$. As electrons undergo bremsstrahlung

1023 energy loss in the tracker material, care is taken to remove from the isolation sums the contributions
 1024 from bremsstrahlung photons and possible resulting conversion electrons.

1025 Electrons are reconstructed from energy deposits in the ECAL matched to tracks reconstructed
 1026 in the silicon tracker. The electron trajectories are reconstructed using a dedicated modeling of the
 1027 electron energy loss and fitted with a Gaussian sum filter. Electrons used in this analysis are required
 1028 to pass the Particle Flow criteria, and to fall in the ECAL pseudorapidity fiducial range ($|\eta| < 2.5$).

1029 The electron identification used in this analysis is based on the “cut-based” Id defined by the
 1030 EGamma POG for the Summer16 25ns [47], and suggested also for the usage in 80X for the so-called
 1031 Moriond dataset. Isolation cuts are already applied within the cut-based Id definitions, therefore
 1032 no additional Isolation cut is required. In the isolation definition the effect of PU is considered by
 1033 taking into account the energy deposits in the calorimeter, estimated through the so-called ρ -area
 1034 method, by subtracting the median energy density in the event ρ multiplied by electron effective
 1035 area. The isolation value is computed in a ΔR cone of 0.3 centered along the lepton direction.

1036 Since in this analysis we are aiming at a final state without any lepton, every electron identified
 1037 with *veto* cut-based Id, transverse momentum $p_T > 10$ GeV is vetoed. The detailed set of cuts to
 1038 define a *veto* cut-based Id electron are reported in the Table 4.1.

	Electrons	Veto	
		EB	EE
$\sigma_{in\eta}$	<	0.0115	0.037
$\Delta\eta_{in}^{seed}$	<	0.00749	0.00895
$\Delta\varphi_{in}$	<	0.228	0.213
H/E	<	0.356	0.211
relIso (EA)	<	0.175	0.159
$ 1/E - 1/p $	<	0.299	0.15
$ d_0 $	<	0.05	0.10
$ d_z $	<	0.10	0.20
missing hits	\leq	2	3
conversion veto	yes	yes	yes

Table 4.1: Summer16 cut-based selection for 25ns conditions. EB: barrel cuts ($|\eta_{supercluster}| \leq 1.479$); EE: endcap cuts ($|\eta_{supercluster}| > 1.479$)

1039 Scale factors for electron identification (including isolation) are provided by Egamma POG, de-
 1040 rived for 80X (Moriond 17 recommendation), that can be found in [48].

1041 4.2.3 Muons

1042 How the muons are reconstructed

1043 In the standard CMS reconstruction for pp collisions, muon tracks are first reconstructed in-
 1044 dependently in the inner tracker (tracker track) and in the muon system (standalone-muon track).
 1045 Based on these objects, two reconstruction approaches are used [49]: *Global Muon* (outside-in) and
 1046 *Tracker Muon* (inside-out).

1048 *reconstruction (outside-in)*: for each standalone-muon track, a matching tracker track is found by comparing parame-
 1049 ters of the two tracks propagated onto a common surface, and a global-muon track is fitted
 1050 combining hits from the tracker track and standalone-muon track, using the Kalman-filter
 1051 technique [50]. At large transverse momenta, $p_T > 200$ GeV, the global-muon fit can improve
 the momentum resolution compared to the tracker-only fit.

4.2 Event selection

reconstruction (*inside-out*): in this approach, all tracker tracks with $p_T > 0.5\text{GeV}$ and the total momentum $p > 2.5\text{GeV}$ are considered as possible muon candidates and are extrapolated to the muon system taking into account the magnetic field, the average expected energy losses, and multiple scattering in the detector material. If at least one muon segment (i.e., a short track stub made of DT or CSC hits) matches the extrapolated track, the corresponding tracker track qualifies as a Tracker Muon.

Tracker Muon reconstruction is more efficient than the Global Muon reconstruction at low momenta, $p_T \lesssim 5\text{GeV}$, because it requires only a single muon segment in the muon system, whereas Global Muon reconstruction is designed to have high efficiency for muons penetrating through more than one muon station and typically requires segments in at least two muon stations. Thanks to the high tracker-track efficiency and a very high efficiency of reconstructing segments in the muon system, about 99% of muons produced in pp collisions and having sufficiently high momentum are reconstructed either as a Global Muon or a Tracker Muon, and very often as both. Muons reconstructed only as standalone-muon tracks have worse momentum resolution and less favorable collision muon to cosmic-ray muon ratio than the Global and Tracker Muons and are usually not used in physics analyses.

Muons are usually based on the *Particle Flow Muon* selection, considering Global Muon or a Tracker Muon candidates and by applying minimal requirements on the track components in the muon system and taking into account a matching with small energy deposits in the calorimeters.

For muons reconstructed using the PF algorithm, the standard muon isolation is defined as the ratio of the p_T sum of all charged and neutral particle-flow candidates in the event within a cone with a radius of $\Delta R = 0.4$ centered along the lepton direction. Corrections in order to reduce the PU contamination are also applied, using the $\Delta\beta$ method. Charged candidates falling into the cone that are not compatible with the primary vertex are removed from the sum. Additionally, the neutral contribution from PU is estimated to be half the one coming from charged candidates, and this quantity is also subtracted from the total. Eventually, the scalar sum is divided by the lepton p_T itself. The general formula for the standard *particle-flow* isolation is then:

$$I_{rel} = \left[\sum p_T^{\text{ch had}} + \max\left(\sum p_T^{\text{neu had}} + \sum p_T^\gamma - 0.5 \cdot \sum p_T^{\text{pu ch had}}, 0\right) \right] / p_T^\ell$$

where $\sum p_T^{\text{ch had}}$ is the sum of the transverse momenta of the charged hadrons, $\sum p_T^{\text{neu had}}$ is the sum of transverse energies of the neutral hadrons, p_T^γ is the sum of the transverse energy of particle flow photons and $\sum p_T^{\text{pu ch had}}$ is the sum of transverse momenta of the charged particles in the cone of interest but with particles not originating from the primary vertex (for pileup corrections).

In the VZ event selection, all muons identified with the Loose standard id, p_T over 10 GeV, PF isolation below 0.25, $\eta < |\mathbf{2.4}|$ are vetoed.

Scale factors for muon identification and isolation are centrally provided as a function of the muon p_T and η by the Muon POG [51], and are applied consistently in the analysis.

4.2.4 Taus

How the taus are reconstructed

The presence of hadronically-decaying taus only act as veto for the events both in the signal and in the control regions to suppress electroweak backgrounds. The selection criteria for taus are $p_T > 18\text{ GeV}$ and $|\eta| < 2.3$. The Run2 TauPOG recommended identification criteria [52] (`decayModeFinding`, `byLooseCombinedIsolationDeltaBetaCorr3Hits`) are required and applied in order to identify possible tau candidates.

 1086 **4.2.5 Photons**

 1087 **How the photons are reconstructed**

1088 As in the case of tau leptons, a photon veto is applied in the analysis both for the signal and
 1089 the control regions. Events are rejected if they contains one (or more) photon with $p_T > 15$ GeV ,
 1090 $|\eta| < 2.5$, passing the Loose cut-based photon ID. The Loose photon Id is applied as in the EGamma
 1091 POG recommandations for Run2 analyses [53] (tuned on Spring16 25 ns samples). The isolation
 1092 cuts (using the rho-area method for the mitigation of the pileup) and conversion safe electron veto
 1093 are applied. The isolation value is computed in a ΔR cone of 0.3 and is corrected for pileup by
 1094 subtracting the event-by-event energy density (ρ) times an effective area. The applied cut-based
 definition of the Loose photon Id is reported in Table 4.2.

Photons	Loose	
	EB	EE
H/E	<	0.0597
$\sigma_{i\eta i\eta}$	<	0.01031
PF ch.had.iso.(ρ -corr)	<	1.295
PF neu.had.iso.(ρ -corr)	<	$10.910 + 0.0148 p_T + 0.000017 p_T^2$
PF photon iso.(ρ -corr)	<	$5.931 + 0.0163 p_T + 0.000014 p_T^2$
conversion veto	yes	$3.630 + 0.0047 p_T$
		$6.641 + 0.0034 p_T$
		yes

Table 4.2: Photon cut-based Id for Spring16 25ns conditions. EB: barrel cuts ($|\eta_{\text{supercluster}}| \leq 1.479$); EE: endcap cuts ($|\eta_{\text{supercluster}}| > 1.479$)

1095 Scale factors for photon identification (including isolation) are provided by Egamma POG, de-
 1096 rived for 80X (Moriond 17 recommendation), that can be found in [48].
 1097

4.2 Event selection

4.2.6 Jets

How the jets are reconstructed

The latest jet energy corrections are applied to AK4 and AK8 CHS jets, and the tags are Summer16 23Sep2016V3.

In this analysis, jets are considered if the corrected p_T is larger than 30 GeV for AK4 jets and 200GeV for AK8 jets, and lie in the tracker acceptance ($|\eta| < 2.4$). Additionally, AK4 are required to pass *loose* jet identification requirements, AK8 are required to pass *tight* jet identification requirements defined by the JETMET POG for Run2 analyses [54], listed in Table 4.3. AK8 jets are used to reconstruct the hadronically decaying electroweak boson candidate, whilst AK4 jets are used to suppress the contribution of top and QCD background events.

EFFICIENZA di TIGHT ID?

Figure 4.2- 4.4 show the data/simulation comparison after the analysis selections (Tab. ?? without Top cleaning and Event cleaning).

PF Jet ID	loose	tight
Neutral Hadron Fraction	< 0.99	< 0.90
Neutral EM Fraction	< 0.99	< 0.90
Number of Constituents	> 1	> 1
Muon Fraction	-	-
Additionally, for $ \eta < 2.4$		
Charged Hadron Fraction	> 0	> 0
Charged Multiplicity	> 0	> 0
Charged EM Fraction	< 0.99	< 0.99

Table 4.3: *Loose* and *Tight* jet identification requirements for Run2 (Spring16) 25ns conditions.

Figure 4.2: Number of reconstructed AK8 jets after selections.

Figure 4.3: Leading AK8 jet p_T spectra after selections.

Figure 4.4: Leading AK8 jet η spectra after selections.

Since it has been measured that the jet energy resolution (JER) is not the same in data and MC, an additional smearing is applied in simulation, in order to get a better agreement, as suggested by JETMET POG [55].

There are two independent ways to get the smearing. With the scaling method, corrected four-momentum of a reconstructed jet is rescaled with a factor

$$c_{\text{JER}} = 1 + (s_{\text{JER}} - 1) \frac{p_T - p_T^{\text{ptcl}}}{p_T},$$

where p_T is its transverse momentum, p_T^{ptcl} is the transverse momentum of the corresponding jet clustered from generator-level particles, and s_{JER} is the data-to-simulation core resolution scale factor. Factor c_{JER} is truncated at zero, i.e. if it is negative, it is set to zero. This method only works if a well-matched particle-level jet is present and can result in a large shift of the response otherwise. The following requirements are imposed for the matching:

$$\Delta R < R_{\text{cone}}/2, |p_T - p_T^{\text{ptcl}}| < 3\sigma_{\text{JER}}p_T.$$

- 1116 Here R_{cone} is the jet cone size parameter (for instance, 0.4 for AK4 jets) and σ_{JER} is the relative p_T
1117 resolution as measured in simulation.

An alternative approach, which does not require the presence of a matching particle-level jet, is the stochastic smearing. In this case corrected jet four-momentum is rescaled with a factor

$$c_{\text{JER}} = 1 + \mathcal{N}(0, \sigma_{\text{JER}})\sqrt{\max(s_{\text{JER}}^2 - 1, 0)},$$

- 1118 where σ_{JER} and s_{JER} are the relative p_T resolution in simulation and data-to-simulation scale factors,
1119 and $\mathcal{N}(0, \sigma)$ denotes a random number sampled from a normal distribution with a zero mean and
1120 variance σ^2 . As before, scaling factor c_{JER} is truncated at zero. This method only allows to degrade
1121 the resolution.

- 1122 The smearing procedure adopted in this analysis is the hybrid method: when matching particle-
1123 level jet is found, the scaling method is used; otherwise the stochastic smearing is applied. The
1124 smearing coefficients and their errors, provided by JETMET POG, are reported in Tab. 4.4 for 2016
1125 data (tag: Spring1625nsV10).

Jet η	SF
0.0–0.5	1.109 ± 0.008
0.5–0.8	1.138 ± 0.013
0.8–1.1	1.114 ± 0.013
1.1–1.3	1.123 ± 0.024
1.3–1.7	1.084 ± 0.011
1.7–1.9	1.084 ± 0.011
1.9–2.1	1.140 ± 0.047
2.1–2.3	1.067 ± 0.053
2.3–2.5	1.177 ± 0.041
2.5–2.8	1.364 ± 0.039
2.8–3.0	1.857 ± 0.071
3.0–3.2	1.328 ± 0.022
3.2–5.0	1.16 ± 0.029

Table 4.4: Smearing coefficients and JER uncertainties.

4.2 Event selection

4.2.7 Jet mass

The jet mass is the main observable in distinguishing a V-jet from a QCD jet. Jet grooming consists in the suppression of uncorrelated UE/PU (underlying event and pile-up) radiation from the target jet and improves the discrimination pushing the jet mass for QCD jets towards lower values while maintaining the jet mass for V-jets around the boson-mass.

The grooming algorithm considered in this analysis is the following:

Soft-drop: The “soft drop declustering” is a jet substructure technique which recursively removes soft wide-angle radiation from a jet [56]. The soft drop algorithm depends on two parameters: a soft threshold z_{cut} and an angular exponent β . Like any grooming method, soft drop declustering removes wide-angle soft radiation from a jet in order to mitigate the effects of contamination from initial state radiation (ISR), underlying event (UE), and multiple hadron scattering (pileup). Given a jet of radius R_0 with only two constituents, the soft drop procedure removes the softer constituent unless:

$$\frac{\min(p_T^1, p_T^2)}{p_T^1 + p_T^2} > z_{cut} \left(\frac{\Delta R_{12}}{R_0} \right)^\beta$$

By construction, this condition fail for wide-angle soft radiation. The degree of jet grooming is controlled by z_{cut} and β , with $\beta \rightarrow \infty$ returning back an ungroomed jet. The $\beta = 0$ limit of the energy loss is particularly interesting, since it is largely insensitive to the value of the strong coupling constant. The default parameters used by CMS are $\beta = 0$ and $z_{cut} = 0.1$.

The grooming algorithm, **soft-drop**, is used in association with **PUPPI** in order to remove soft and wide-angle radiations and the pile-up contribution. It is a shared choice among all the diboson analyses, praised by theoreticians.

Unfortunately, the default soft-drop + PUPPI jet mass suffers from a systematic shift from the expected value of about $\sim 10\%$, and some residual dependence on the jet p_T . Further corrections to the jet mass have been applied:

Gen: a p_T -dependent correction to account for a small shift in the generated vector boson mass, applied only on simulated samples

Reco: a p_T -dependent correction to the reconstructed jet mass, applied separately for jets in the barrel and endcaps regions

These corrections are evaluated centrally by JMAR and documented in [57], and applied accordingly within the analysis.

Figure 4.6- 4.7 show the jet mass for W or Z bosons before and after the correction, without applying any cut on this variable.

Figure 4.5: Softdrop + PUPPI mass of AK8 jet reconstructed for different bulk graviton signal samples; left: before corrections. right: after corrections.

Furthermore, in order to obtain a better data-Monte Carlo agreement, a smearing procedure has been applied to the puppi softdrop mass, by using the stochastic method, with a constant smearing coefficient provided by JETMET POG (1.00 ± 0.20), that does not depend on jet pseudorapidity if it is restricted to $|\eta| < 2.5$.

Figure 4.6: Softdrop + PUPPI mass of AK8 jet reconstructed for different W' signal samples; left: before corrections. right: after corrections.

Figure 4.7: Softdrop + PUPPI mass of AK8 jet; left: before corrections. right: after corrections.

1154 **4.2.8 Jet substructure**

In order to further discriminate signal from background, it is useful to investigate the inner structure of the jet. Studying the distribution of the jet constituents with respect to the jet axis allows us to test the hypothesis of the existence of multiple substructures, that could be evidence of jets originated by more than one parton. This procedure proceeds as follows: the constituents of the jet are clustered again with the k_T algorithm, however the procedure is stopped when one obtains N subjets. Then, a new variable, the N-subjettiness, is introduced. It is defined as:

$$\tau_N = \frac{1}{d_0} \sum_k p_{T,k} \min(\Delta R_{1,k}^\beta, \Delta R_{2,k}^\beta, \dots, \Delta R_{N,k}^\beta)$$

1155 where β is an arbitrary parameter, the index k runs over the jet constituents and the distances $\Delta R_{N,k}$
1156 are calculated with respect to the axis of the N-th subjet, obtained by one iteration of τ minimization
1157 by varying the subjet axes around the k_T subjet axes.

The normalization factor d_0 is calculated as $d_0 = \sum_k p_{T,k} R_0^\beta$, setting R_0 to the radius of the original jet. The N-subjettiness is always included in the interval from 0 to 1 and represents the compatibility of the jet structure with an N-subjet hypothesis: small values correspond to high compatibility. Indeed, τ_N weights the transverse momentum of the jet constituents by their angular distance to the closest subjet. In this analysis the N-subjettiness is calculated from the ungroomed jet with the parameter $\beta = 1$. The subjettiness related to the one and two subjet hypothesis is thus:

$$\tau_1 = \frac{1}{d_0} \sum_k p_{T,k} \Delta R_{1,k}$$

and

$$\tau_2 = \frac{1}{d_0} \sum_k p_{T,k} \min(\Delta R_{1,k}, \Delta R_{2,k})$$

1158 In principle, these two quantities should allow us to distinguish the dipole-like nature of the showering of the Higgs decay from the classic monopole structure of QCD jets. In particular, the variable
1159 that best discriminates between V-jets and QCD jets is the ratio of 2-subjettiness and 1-subjettiness,
1160
1161 $\tau_{21} = \tau_2 / \tau_1$.

1162 Figure 4.8 shows the τ_{21} distributions for the PUPPI algorithm.

Figure 4.8: τ_{21} subjettiness of PUPPI AK8 jet after inclusive selections.

1163 **4.2.9 b-tagging**

1164 B-tagging algorithms are applied to both the fat-jet and the sub-jets, independently. For subjets,
1165 run-II taggers are by default applied on the same charged particle-flow candidate list that is used

4.2 Event selection

in the jet clustering (*explicit jet-to-track association*). Thanks to the explicit jet-to-track association, the two sub-jets do not share any PF-constituent, avoiding unintended correlations.

The jet or sub-jet is considered as tagged if the discriminator value is above some threshold value, often referred to as the cut value, and the efficiency is defined as the number of jets which have a discriminator value that is above that cut divided by the total number of jets (of the same flavor).

The b-tagging algorithm used to set the analysis strategy is the Combined Secondary Vertex (CSV) [58] discriminator (full name `pfCombinedInclusiveSecondaryVertexV2BJetTags`). Different working points are provided by the POG for Run2 analyses [59], as shown in table 4.2.9, but the only one used in this analysis is the *loose* working point.

Working point	CSV cut	mis-tag probability
CSVL (Loose)	> 0.5426	≈ 10%
CSVM (Medium)	> 0.8484	≈ 1%
CSVT (Tight)	> 0.9535	≈ 0.1%

Table 4.5: Working point for CSV b-tagging algorithm.

B-tagging efficiency is not the same in data and MC. In order to take into account this difference, the BTV POG provides collections of b-tagging scale factors for b-jets and mistagged light jets, measured for different physics processes, for the supported tagging algorithms and the three standard working points [58]. A weight is calculated on a per-event basis as a function of the b-tagging status of the jets and their kinematic variables [60].

In this analysis, b-tagging is used in order to reject events where a top quark is involved, by asking to the AK4 jets not laying in the AK8 jet cone to be anti b-tagged (in practice, the maximum CSV value allowed is the loose working point, CSVL).

4.2.10 Missing Energy

How the MET is reconstructed

The E_T^{miss} is the imbalance in the transverse momentum of all visible particles, and it is reconstructed with the particle flow algorithm [61]. The *raw* E_T^{miss} is defined as the inverse vectorial sum of the transverse momentum of all the reconstructed charged and neutral particle flow candidates: $E_T^{\text{miss}} = -\sum_{i=0}^{\text{all}} \vec{p}_{T,i}$. The raw E_T^{miss} is systematically different from true E_T^{miss} , for many reasons including the non-compensating nature of the calorimeters and detector misalignment. To better estimate the true E_T^{miss} , corrections can be applied:

Type-0: a mitigation for the degradation of the E_T^{miss} reconstruction due to the pileup interactions, by applying the CHS algorithm. However, the E_T^{miss} contribution from pileup neutral particles cannot be easily subtracted; the assumption is that the E_T^{miss} contribution term of charged and neutral pileup particles are the same, and cancellation at the true level is exact: $\sum_{\text{neuPU}} \vec{p}_{T,i}^{\text{true}} + \sum_{\text{chPU}} \vec{p}_{T,i}^{\text{true}} = 0$. An additional E_T^{miss} term is then added to the raw E_T^{miss} to take into account the neutral PU contribution, which is equal to the charged one with a multiplicative scale factor taking into account calorimeter mismeasurements of low- p_T energy deposits.

Type-1: propagation of the jet energy corrections (JEC) to MET. The Type-I correction replaces the vector sum of transverse momenta of particles which can be clustered as jets with the vector sum of the transverse momenta of the jets to which JEC is applied.

Particle flow E_T^{miss} with type-1 corrections applied is currently the default one used by CMS physics analyses. Additionally, some E_T^{miss} filters have been recommended by JETMET POG for Run2 analy-

1204 ses [54], in order to remove events with spurious E_T^{miss} related to detector noise and bad reconstructions,
 1205 and they are listed in sec. ??.

1206 Since the E_T^{miss} corrections and uncertainties depend on the JEC applied, they are re-computed
 1207 accordingly following the JETMETPOG recommendation:

```
1208 from PhysicsTools.PatUtils.tools.runMETCorrectionsAndUncertainties import
1209 runMetCorAndUncFromMiniAOD
1210 # If you only want to re-correct and get the proper uncertainties
1211 runMetCorAndUncFromMiniAOD(process,
1212                         isData=True (or False),
1213                         )
1214 process.p = cms.Path(process.fullPatMetSequence *
1215                         process.yourAnalyzer)
1216
1217 cms.InputTag("slimmedMETS","","YourProcessName")
```

1218 Figure 4.9 show the E_T^{miss} distribution for data and Monte Carlo after the corrections and filters.

Figure 4.9: Type-1 corrected E_T^{miss} distribution after inclusive selections.

¹²¹⁹ **4.3 Diboson candidate reconstruction**

₁₂₂₀ **4.4 Background estimation**

4.5 Systematic uncertainties

1221 4.5 Systematic uncertainties

₁₂₂₂ **4.6 Results**

Combination of diboson searches in semileptonic final states

Conclusions

1227

1228

1229

Bibliography

1230

1231

- 1232 [1] G. Aad *et al.*, “Observation of a new particle in the search for the Standard Model Higgs boson
1233 with the ATLAS detector at the LHC,” *Phys. Lett. B*, vol. 716, p. 1, 2012.
- 1234 [2] S. Chatrchyan *et al.*, “Observation of a new boson at a mass of 125 GeV with the CMS experi-
1235 ment at the LHC,” *Phys. Lett. B*, vol. 716, p. 30, 2012.
- 1236 [3] S. Chatrchyan *et al.*, “Observation of a new boson with mass near 125 GeV in pp collisions at
1237 $\sqrt{s} = 7$ and 8 TeV,” *JHEP*, vol. 06, p. 081, 2013.
- 1238 [4] G. Aad *et al.*, “Evidence for the spin-0 nature of the Higgs boson using ATLAS data,” *Phys. Lett.*
1239 *B*, vol. 726, p. 120, 2013.
- 1240 [5] V. Khachatryan *et al.*, “Precise determination of the mass of the Higgs boson and tests of com-
1241 patibility of its couplings with the standard model predictions using proton collisions at 7 and
1242 8 TeV,” *Eur. Phys. J. C*, vol. 75, p. 212, 2015.
- 1243 [6] G. Aad *et al.*, “Measurement of the Higgs boson mass from the $H \rightarrow \gamma\gamma$ and $H \rightarrow ZZ^* \rightarrow 4\ell$
1244 channels in pp collisions at center-of-mass energies of 7 and 8 TeV with the ATLAS detector,”
1245 *Phys. Rev. D*, vol. 90, p. 052004, 2014.
- 1246 [7] CMS and ATLAS Collaborations, “Combined Measurement of the Higgs Boson Mass in pp Col-
1247 lisions at $\sqrt{s} = 7$ and 8 TeV with the ATLAS and CMS Experiments.” Submitted to *Phys. Rev. Lett.*,
1248 2015.
- 1249 [8] G. Degrassi, S. Di Vita, J. Elias-Miro, J. R. Espinosa, G. F. Giudice, G. Isidori, and A. Strumia,
1250 “Higgs mass and vacuum stability in the Standard Model at NNLO,” *JHEP*, vol. 08, p. 098, 2012.
- 1251 [9] D. Pappadopulo, A. Thamm, R. Torre, and A. Wulzer, “Heavy vector triplets: bridging theory
1252 and data,” *Journal of High Energy Physics*, vol. 2014, no. 9, pp. 1–50, 2014.
- 1253 [10] V. D. Barger, W.-Y. Keung, and E. Ma, “A Gauge Model With Light W and Z Bosons,” *Phys. Rev.*,
1254 vol. D22, p. 727, 1980.
- 1255 [11] C. Grojean, E. Salvioni, and R. Torre, “A weakly constrained W' at the early LHC,” *JHEP*, vol. 07,
1256 p. 002, 2011.

- 1257 [12] R. Contino, D. Pappadopulo, D. Marzocca, and R. Rattazzi, “On the effect of resonances in com-
1258 posite higgs phenomenology,” *Journal of High Energy Physics*, vol. 2011, no. 10, pp. 1–50, 2011.
- 1259 [13] B. Bellazzini, C. Csáki, and J. Serra, “Composite Higgses,” *Eur. Phys. J.*, vol. C74, no. 5, p. 2766,
1260 2014.
- 1261 [14] G. F. Giudice, C. Grojean, A. Pomarol, and R. Rattazzi, “The Strongly-Interacting Light Higgs,”
1262 *JHEP*, vol. 06, p. 045, 2007.
- 1263 [15] A. Wulzer, “An Equivalent Gauge and the Equivalence Theorem,” *Nucl. Phys.*, vol. B885,
1264 pp. 97–126, 2014.
- 1265 [16] A. M. Sirunyan *et al.*, “Search for massive resonances decaying into WW, WZ, ZZ, qW, and qZ
1266 with dijet final states at $\sqrt{s} = 13$ TeV,” 2017.
- 1267 [17] CMS Collaboration, “Search for massive resonances decaying into WW, WZ, ZZ, qW and qZ in
1268 the dijet final state at $\sqrt{s} = 13$ TeV,” CMS Physics Analysis Summary CMS-PAS-B2G-17-001,
1269 CERN, Geneva, 2017.
- 1270 [18] C. Collaboration, “Search for heavy resonances decaying into a vector boson and a Higgs boson
1271 in hadronic final states with 2016 data,” 2017.
- 1272 [19] CMS Collaboration, “Search for heavy resonances decaying into a vector boson and a Higgs bo-
1273 son in hadronic final states with 2016 data,” CMS Physics Analysis Summary CMS-PAS-B2G-17-
1274 002, CERN, Geneva, 2017.
- 1275 [20] CMS Collaboration, “Search for heavy resonances decaying into a Z boson and a W boson in
1276 the $\ell^+\ell^-q\bar{q}$ final state,” CMS Physics Analysis Summary CMS-PAS-B2G-16-022, CERN, Geneva,
1277 2017.
- 1278 [21] V. Khachatryan *et al.*, “Search for heavy resonances decaying into a vector boson and a Higgs
1279 boson in final states with charged leptons, neutrinos, and b quarks,” *Phys. Lett.*, vol. B768,
1280 pp. 137–162, 2017.
- 1281 [22] CMS Collaboration, “Search for new resonances decaying to $WW/WZ \rightarrow \ell\nu qq$,” CMS Physics
1282 Analysis Summary CMS-PAS-B2G-16-020, CERN, Geneva, 2016.
- 1283 [23] CMS Collaboration, “Search for heavy resonances decaying into a Z boson and a vector bo-
1284 son in the $\nu\nu q\bar{q}$ final state,” CMS Physics Analysis Summary CMS-PAS-B2G-17-005, CERN,
1285 Geneva, 2017.
- 1286 [24] M. Aaboud *et al.*, “Search for diboson resonances with boson-tagged jets in pp collisions at
1287 $\sqrt{s} = 13$ TeV with the ATLAS detector,” 2017.
- 1288 [25] ATLAS Collaboration, “Search for WW/WZ resonance production in $\ell\nu qq$ final states in pp
1289 collisions at $\sqrt{s} = 13$ TeV with the ATLAS detector,” ATLAS Conference Note ATLAS-CONF-
1290 2017-051, CERN, Geneva, Jul 2017.
- 1291 [26] “Searches for heavy ZZ and ZW resonances in the llqq and vvqq final states in pp collisions
1292 at $\sqrt{s} = 13$ TeV with the ATLAS detector,” ATLAS Conference Note ATLAS-CONF-2016-082,
1293 CERN, Geneva, Aug 2016.
- 1294 [27] M. Aaboud *et al.*, “Search for heavy resonances decaying to a W or Z boson and a Higgs boson
1295 in the $q\bar{q}^{(\prime)}b\bar{b}$ final state in pp collisions at $\sqrt{s} = 13$ TeV with the ATLAS detector,” 2017.

BIBLIOGRAPHY

- 1296 [28] ATLAS Collaboration, “Search for heavy resonances decaying to a W or Z boson and a Higgs
1297 boson in final states with leptons and b -jets in 36.1 fb^{-1} of $p p$ collision data at $\sqrt{s} = 13 \text{ TeV}$
1298 with the ATLAS detector,” ATLAS Conference Note ATLAS-CONF-2017-055, CERN, Geneva, Jul
1299 2017.
- 1300 [29] L. Randall and R. Sundrum, “A Large mass hierarchy from a small extra dimension,” *Phys. Rev.*
1301 *Lett.*, vol. 83, pp. 3370–3373, 1999.
- 1302 [30] L. Randall and R. Sundrum, “An Alternative to compactification,” *Phys. Rev. Lett.*, vol. 83,
1303 pp. 4690–4693, 1999.
- 1304 [31] K. Agashe, H. Davoudiasl, G. Perez, and A. Soni, “Warped Gravitons at the LHC and Beyond,”
1305 *Phys. Rev.*, vol. D76, p. 036006, 2007.
- 1306 [32] A. L. Fitzpatrick, J. Kaplan, L. Randall, and L.-T. Wang, “Searching for the Kaluza-Klein Graviton
1307 in Bulk RS Models,” *JHEP*, vol. 09, p. 013, 2007.
- 1308 [33] H. Davoudiasl, J. L. Hewett, and T. G. Rizzo, “Phenomenology of the Randall-Sundrum Gauge
1309 Hierarchy Model,” *Phys. Rev. Lett.*, vol. 84, p. 2080, 2000.
- 1310 [34] T. Gherghetta and A. Pomarol, “Bulk fields and supersymmetry in a slice of AdS,” *Nucl. Phys.*,
1311 vol. B586, pp. 141–162, 2000.
- 1312 [35] H. Davoudiasl, J. L. Hewett, and T. G. Rizzo, “Experimental probes of localized gravity: On and
1313 off the wall,” *Phys. Rev.*, vol. D63, p. 075004, 2001.
- 1314 [36] A. Oliveira, “Gravity particles from Warped Extra Dimensions, predictions for LHC,” 2014.
- 1315 [37] CMS Collaboration, “Search for diboson resonances in the $2l2\nu$ final state,” CMS Physics Analysis
1316 Summary CMS-PAS-B2G-16-023, CERN, Geneva, 2017.
- 1317 [38] CMS Collaboration, “Search for heavy resonances decaying to a pair of Higgs bosons in the four
1318 b quark final state in proton-proton collisions at $\sqrt{s} = 13 \text{ TeV}$,” CMS Physics Analysis Summary
1319 CMS-PAS-B2G-16-026, CERN, Geneva, 2017.
- 1320 [39] “Pileup Removal Algorithms,” Tech. Rep. CMS-PAS-JME-14-001, CERN, Geneva, 2014.
- 1321 [40] M. Cacciari, G. P. Salam, and G. Soyez, “The anti- k_t jet clustering algorithm,” *JHEP*, vol. 04,
1322 p. 063, 2008.
- 1323 [41] T. C. collaboration, “Determination of jet energy calibration and transverse momentum reso-
1324 lution in cms,” *Journal of Instrumentation*, vol. 6, no. 11, p. P11002, 2011.
- 1325 [42] S. Chatrchyan *et al.*, “Performance of tau-lepton reconstruction and identification in CMS,”
1326 *JINST*, vol. 7, p. P01001, 2012.
- 1327 [43] CMS Collaboration, “Identification of b quark jets at the CMS Experiment in the LHC Run 2,”
1328 CMS Physics Analysis Summary CMS-PAS-BTV-15-001, CERN, Geneva, 2016.
- 1329 [44] S. Chatrchyan *et al.*, “Identification of b -quark jets with the CMS experiment,” *JINST*, vol. 8,
1330 p. P04013, 2013.
- 1331 [45] “Pileup Reweighting Procedure - <https://twiki.cern.ch/twiki/bin/viewauth/CMS/PileupReweighting>,”
1332

- 1333 [46] “Utilities for Accessing Pileup Information for Data - <https://twiki.cern.ch/twiki/bin/view/CMS/PileupJSONFileforData>,”
- 1334
- 1335 [47] “EGamma POG - Cut based electron ID for Run2 - <https://twiki.cern.ch/twiki/bin/view/CMS/CutBasedElectronIdentificationRun2>,”
- 1336
- 1337 [48] “EGamma POG - Electron ID recipes for Run2 - <https://twiki.cern.ch/twiki/bin/view/CMS/EgammaIDRecipesRun2>,”
- 1338
- 1339 [49] CMS Collaboration, “Performance of cms muon reconstruction in pp collision events at $\sqrt{s} = 7\text{TeV}$.” Submitted to *J. Inst.*, 2012.
- 1340
- 1341 [50] R. Fruhwirth, “Application of kalman filtering to track and vertex fitting,” *Nuclear Instruments and Methods in Physics Research Section A: Accelerators, Spectrometers, Detectors and Associated Equipment*, vol. 262, no. 23, pp. 444 – 450, 1987.
- 1342
- 1343
- 1344 [51] “Reference muon id, isolation and trigger efficiencies for Run-II - <https://twiki.cern.ch/twiki/bin/view/CMS/MuonReferenceEffsRun2>,”
- 1345
- 1346 [52] “Tau POG - Tau ID for Run2 - <https://twiki.cern.ch/twiki/bin/viewauth/CMS/TauIDRecommendation13TeV>,”
- 1347
- 1348 [53] “EGamma POG - Cut based photon ID for Run2 - <https://twiki.cern.ch/twiki/bin/view/CMS/-CutBasedPhotonIdentificationRun2>,”
- 1349
- 1350 [54] “JetMET POG - Jet ID for Run2 - <https://twiki.cern.ch/twiki/bin/view/CMS/JetID>,”
- 1351 [55] “Jetmet pog - jet energy resolution smearing - <https://twiki.cern.ch/twiki/bin/view/cms/jetresolution>,”
- 1352
- 1353 [56] A. J. Larkoski, S. Marzani, G. Soyez, and J. Thaler, “Soft Drop,” *JHEP*, vol. 05, p. 146, 2014.
- 1354 [57] T. K. Arrestad et al., “Identification and calibration of boosted hadronic W/Z bosons at 13 TeV,” tech. rep., AN-2016/215, 2016.
- 1355
- 1356 [58] S. Chatrchyan *et al.*, “Identification of b-quark jets with the CMS experiment,” *JINST*, vol. 8, p. P04013, 2013.
- 1357
- 1358 [59] “BTV POG - B-tagging for Run2 - <https://twiki.cern.ch/twiki/bin/view/CMS/BtagRecommendation80X>,”
- 1359
- 1360 [60] “Methods to apply b-tagging efficiency scale factors,” 2013.
- 1361 [61] CMS Collaboration, “Particle-flow event reconstruction in CMS and performance for jets, taus, and E_T^{miss} ,” no. CMS-PAS-PFT-09-001, 2009.
- 1362